Biophysical Journal
Article

Biophysical Society

An integrated multiscale computational framework deciphers SARS-CoV-2 resistance to sotrovimab

Akshit Sharma,[1] Shweata Maurya,[1] Shivank Kumar,[1] Timir Tripathi,[2,*] Rajiv K. Kar,[3,4,*] and Aditya K. Padhi[1,*]
[1]Laboratory for Computational Biology & Biomolecular Design, School of Biochemical Engineering, Indian Institute of Technology (BHU), Varanasi, Uttar Pradesh 221005, India; [2]Molecular and Structural Biophysics Laboratory, Department of Zoology, North-Eastern Hill University, Shillong, India; [3]Jyoti and Bhupat Mehta School of Health Sciences and Technology, Indian Institute of Technology Guwahati, Guwahati, Assam, India; and [4]Centre for Nanotechnology, Indian Institute of Technology Guwahati, Guwahati, Assam, India

ABSTRACT The emergence of resistance mutations in the SARS-CoV-2 spike (S) protein presents a challenge for monoclonal antibody treatments like sotrovimab. Understanding the structural, dynamic, and molecular features of these mutations is essential for therapeutic advancements. However, the intricate landscape of potential mutations and critical residues conferring resistance to mAbs like sotrovimab remains elusive. This study introduces an integrated framework that combines interface protein design, machine learning, hybrid quantum mechanics/molecular mechanics methodologies, all-atom and coarse-grained molecular dynamics simulations, and correlation analysis. Beginning with the interface-based design and analysis, this framework elucidates the interaction between sotrovimab and the S-protein, identifying pivotal residues and plausible resistance mutations. Machine learning algorithms then facilitate the identification of potential resistance mutations using structural-sequence-binding affinity-energetics features. The hybrid quantum mechanics/molecular mechanics approach subsequently evaluates the role of mutational residues as quantum regions, assessing their impact on stabilizing the macromolecular complex. To gain a deeper understanding of the dynamic behavior of these mutations, multiscale simulations comprising all-atom and coarse-grained molecular dynamics simulations were performed, revealing their structural, biophysical and energetic impacts. These simulations complemented the static predictions, capturing the conformational dynamics and stability of the mutants in presence of glycan in the S-protein. The accuracy of the predictions is validated by correlating identified resistance mutations with clinical-sequencing data and empirical evidence from sotrovimab-treated patients. Notably, two residues, E340 at the S-protein-sotrovimab interface and Y508 distal from it, and their designs, align with clinically observed resistance mutations. Furthermore, machine learning approaches predict novel S-protein sequences with enhanced/reduced affinity for sotrovimab, validated structurally using AlphaFold. This integrated framework showcases its effectiveness in identifying potential resistance mutations, corroborated with clinical insights and offering a multidimensional strategy for decoding resistance mutations in SARS-CoV-2. Its translational relevance extends to understanding resistance mechanisms and designing novel antibody therapeutics in other systems.

SIGNIFICANCE This study presents an integrated multiscale computational framework to explore SARS-CoV-2 resistance to monoclonal antibody sotrovimab. By combining computational protein design, machine learning, hybrid quantum mechanics/molecular mechanics simulations, all-atom and coarse-grained molecular dynamics simulations, the framework optimizes sotrovimab's interaction with the spike protein receptor-binding domain and, eventually, identifies resistance mutations including known ones like E340A/D/K/Q/V in the receptor-binding domain. It provides critical insights into their biophysical impacts along with corroboration with clinical results. These findings underscore the potential of computational frameworks in overcoming antibody resistance and advancing therapeutics strategies to combat rapidly evolving pathogens like SARS-CoV-2.

INTRODUCTION

The postpandemic impact of COVID-19 continues to be a global concern, with emerging SARS-CoV-2 variants evolving due to genetic mutations (1). These mutations impact the effectiveness of current drugs and monoclonal antibody (mAb) treatments, necessitating continuous

Submitted December 11, 2024, and accepted for publication May 14, 2025.

*Correspondence: timir.tripathi@gmail.com or rajivkar@iitg.ac.in or aditya.bce@iitbhu.ac.in

Akshit Sharma and Shweata Maurya contributed equally to this work.

Editor: Abhishek Singharoy.

https://doi.org/10.1016/j.bpj.2025.05.015

surveillance and adaptation. Variants like Alpha (B.1.1.7), Beta (B.1.351), Gamma (P.1), Delta (B.1.617.2), and the emerging Omicron (B.1.1.529), particularly its subvariant JN.1, raise concerns due to their rapid spread and mutations in critical protein domains (1). Addressing these variants poses challenges for antiviral drug development, as genetic changes can compromise drug efficacy and foster resistance. Antiviral drugs like remdesivir, favipiravir, nirmatrelvir, and molnupiravir and mAb therapies such as bamlanivimab, casirivimab/imdevimab, bebtelovimab, and sotrovimab face challenges posed by viral evolution and resistance mechanisms, emphasizing the need for ongoing surveillance and adaptive strategies (2–6).

Sotrovimab (VIR-7831) is one such mAb that has exhibited potential in combating SARS-CoV-2 infection and reducing the severity of COVID-19 symptoms (7). By binding to the spike (S)-protein receptor-binding domain (RBD), sotrovimab obstructs viral attachment and entry, thereby, impeding disease progression. Clinical trials evaluating the efficacy and safety of sotrovimab have yielded promising results (8). The COMET-ICE trial examined the use of sotrovimab in high-risk nonhospitalized individuals with mild-to-moderate COVID-19, demonstrating a substantial reduction in hospitalization or death (9,10). Furthermore, the ACTIV-3/TICO RECOVERY trial indicated a potential benefit in reducing the risk of death or the need for mechanical ventilation in patients receiving sotrovimab (11,12). In 2021, sotrovimab received emergency use authorization from the US FDA to treat high-risk patients susceptible to progressing to severe COVID-19 (13,14). Moreover, promising data suggested that sotrovimab retains its neutralizing activity against several variants of SARS-CoV-2, including Alpha, Beta, Gamma, and Delta (15–17). This broad-spectrum neutralization capability is crucial in the face of viral evolution and the emergence of variants that may exhibit reduced susceptibility to other therapeutics (18). By effectively neutralizing a wide range of variants, sotrovimab holds promise as a therapeutic option even in the presence of viral mutations (19,20). Another critical aspect of sotrovimab's mechanism of action is its potential to reduce the risk of viral escape through resistance mutations. Studies have revealed that the binding site of sotrovimab on the RBD overlaps with regions prone to mutations associated with antibody resistance (21). This suggests that the development of resistance to sotrovimab may necessitate significant mutations that could potentially impact viral fitness. Hence, the multifaceted mechanism of action of sotrovimab may provide a higher barrier for resistance development compared with antibodies targeting other epitopes.

However, the continuous evolution of the SARS-CoV-2 poses a threat to sotrovimab's efficacy due to reported resistance mutations emerging in its primary target, the RBD of the S-protein (22). These mutations have been observed in immunocompromised patients after sotrovimab treatment, raising concerns about its long-term effectiveness. However, a comprehensive understanding of all potential resistance mutations remains elusive. To address this, Greaney et al. (2021) proposed a method to identify SARS-CoV-2 RBD mutants using experimental approaches, though these methods are time and resource-intensive, especially during outbreaks (23). In contrast, efficient computational methods can predict mutation hotspots relatively quickly that offer the virus a selective advantage. A grasp of resistance mechanisms is vital for shaping therapeutic strategies and advancing next-generation antibody treatments, foreseeing concerning variants before they spread widely (24).

Taking these factors into account, we have devised an integrated multiscale computational framework for deciphering resistance mutations in the SARS-CoV-2 S-protein against not only sotrovimab but also any other mAb with analogous binding characteristics (25,26). This framework integrates computational protein design (CPD), machine learning (ML) algorithms, hybrid quantum mechanics/molecular mechanics (QM/MM) simulations, all-atom and coarse-grained molecular dynamics (MD) simulations, RBD sequence predictions with enhanced/reduced binding affinities, structural validation using AlphaFold, and correlation analysis with clinical records and sequencing data, resulting in a thorough grasp of viral resistance mechanisms. To illustrate the effectiveness of our framework, we investigated mutations of two clinically reported resistance-causing S-protein residues: E340, situated at the sotrovimab-binding juncture, and Y508, positioned distantly (27–29). By linking computational insights and predictions with real-world clinical evidence, we highlight the potential of our framework in obtaining a cohesive and comprehensive picture of resistance mutations and guiding treatment strategies in the ongoing combat against COVID-19 and possible future epidemics.

MATERIALS AND METHODS

Computational design of sotrovimab-resistant S-protein mutants

To identify sotrovimab-resistance mutations in the SARS-CoV-2 S-protein RBD, we employed a combined ResScan-design and Rosetta-based interface design approach. The x-ray crystal structure of the Omicron variant bound to sotrovimab (PDB: 7TLY) was used as the structural template (Fig. 1 *A*) (30). The Molecular Operating Environment (MOE, version 2022.03) was utilized for structure preparation, followed by identification of sotrovimab-interacting residues within the RBD (31).

ResScan-design approach

Using the ResScan-design protocol, a library of amino acid mutations was generated to model potential resistance-conferring mutations in the S-protein (32–34). Mutations were introduced at sotrovimab-binding residues and sampled using naturally occurring single nucleotide polymorphisms (SNPs) that have minimal or nondamaging effects on the virus (32). The ensemble protein design module of ResScan-design was used

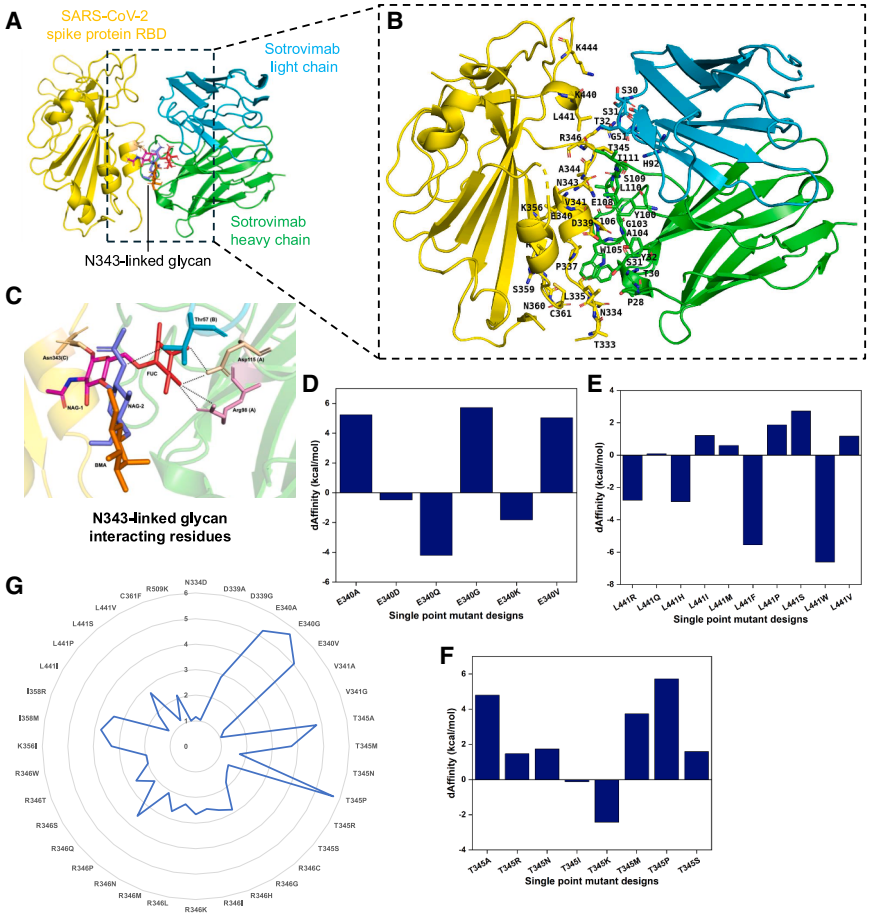

FIGURE 1 Structure of the sotrovimab-S-protein-RBD-glycan complex and relative binding affinities of sotrovimab-S-protein-RBD computed from ResScan-design. (*A*) The cartoon represents the complex structure of SARS-CoV-2 S-protein RBD bound to sotrovimab, which illustrates the intricate interaction between the heavy and light chains of sotrovimab with the S-protein-RBD of SARS-CoV-2. The N343-linked glycan is shown as stick model. (*B*) The detailed interactions between the interface residues of the S-protein-RBD that directly engage with both the heavy and light chains of sotrovimab are shown as stick models and labeled. (*C*) The N343-glycan interacting residues of RBD and sotrovimab are shown, where black dashed lines show polar interactions. (*D* and *F*) represent the dAffinity values (positive and higher relative binding affinities), suggesting that the mutations at positions E340 and E345 resulted in a reduction in binding affinity between sotrovimab and S-protein-RBD. Conversely, in (*E*), lower dAffinity values (negative changes in relative binding affinity) were observed, indicating an increased binding affinity between the designs of S-protein-RBD with sotrovimab at the L441 position. In (*G*), a radar plot is shown depicting the designs that experienced dAffinity of >1 kcal/mol. The corresponding dAffinity values of these designs are indicated on the plot. These designs have the highest possibility of developing resistance to sotrovimab as a result of high dAffinity values as computed from the ResScan-design protocol.

to create 1191 designs across 136 residues of the S-protein, incorporating backbone flexibility (root-mean-squared deviation (RMSD) cutoff: 0.5 Å), and using default parameters were set for other factors such as energy window, fix residues farther than, and conformation limit (10 kcal/mol, 4.5 Å, and 25 K, respectively). The relative binding affinity of the mutant S-protein to sotrovimab was quantified as dAffinity, representing the Boltzmann-averaged binding energies of the designed ensembles (35). This approach provided an indirect computational fitness assessment, sampling only nondeleterious mutations that are more likely to occur in natural settings.

Rosetta-based interface design

For structural refinement and interface design, the MOE-derived S-protein-RBD-sotrovimab complex was further optimized using Rosetta's relax protocol (36,37), generating multiple low-energy structures. The Rosetta macromolecular modeling suite was then employed to redesign sotrovimab-interacting residues while incorporating backbone flexibility (38). In this process, 136 residues were redesigned using naturally occurring SNPs, whereas noninteracting residues were repacked to maintain structural stability. A modified RosettaScript was implemented to account for backbone movements and prevent steric clashes with sotrovimab postmutation (39,40). A total of 100,000 designed complexes were generated and assessed based on Rosetta total score, RMSD from the initial structure, Rosetta interface ΔΔG (binding affinity between the designed S-protein and sotrovimab), and percentage sequence identity with the original S-protein. To further analyze mutational trends, WebLogo was used to visualize the frequency and type of designed mutations across the 136 sotrovimab-binding residues, providing insights into the structural and functional implications of resistance-conferring mutations (41). By integrating ResScan-design and Rosetta-based CPD approaches, we systematically explored the mutational landscape of sotrovimab resistance, identifying key mutations that may alter binding affinity and contribute to viral escape.

Machine-learning-based prediction of sotrovimab resistance mutations, novel RBD sequences and AlphaFold-based structural modeling

To complement design predictions and overcome the constraint of relying solely on structural information for predicting resistance mutations, we employed ML algorithms to identify SARS-CoV-2 S-protein mutations conferring sotrovimab resistance. A comprehensive data set was curated, incorporating wild-type (WT) and resistance mutations alongside features such as CPD-generated designs, protein-protein interaction attributes (e.g., number of interfacial contacts, noninteracting surfaces (NISs), predicted binding affinity (ΔG), dissociation constant (K_d) as obtained using PRODIGY) (42), and various physicochemical properties such as Affinity, dAffinity, Stability, and dStability (from CPD-generated designs). Similarly, contact-based features such as number of intermolecular contacts, number of charged-charged contacts, number of charged-polar contacts, number of charged-apolar contacts, number of polar-polar contacts, number of apolar-polar contacts, number of apolar-apolar contacts, percentage of apolar NIS residues, percentage of charged NIS residues, ΔG (kcal/mol), and K_d (M) at 25°C were derived using PRODIGY. The data set was preprocessed using OneHotEncoder for categorical amino acid features and split

into training (80%) and test (20%) sets (43,44). Three regression models—linear regression, decision tree regression, and XGBoost—were evaluated, with XGBoost ultimately selected for optimal performance (45). Hyperparameter tuning was conducted using GridSearchCV (46), and model accuracy was assessed via 10-fold cross-validation, using the R^2 regression score (ranging from 0 to 1) to measure correlation with CPD-derived binding affinity. Resistance mutations were validated by comparing ML predictions with CPD results and experimental data, and feature importance analysis provided insights into key determinants of sotrovimab resistance.

Here,

$$R^2 = 1 - \frac{\text{Sum squared regression (SSR)}}{\text{Total sum of squares (SST)}}$$

$$R^2 = 1 - \frac{\sum (y_i - y_j)^2}{\sum (y_i - y_k)^2}$$

Where, y_i = actual target values, y_j = predicted target values, and y_k = mean of actual target values.

To further predict novel SARS-CoV-2 RBD sequences that enhance or reduce sotrovimab binding, we developed a multiclass-multioutput random forest regression model. This model integrated 136 designed positions with CPD data (47), predicting sequences with varying binding affinities. Using Rosetta interface ΔΔG scores, we identified affinity-enhancing and affinity-reducing sequences, aiding therapeutic strategies. The ML-predicted sequences were structurally validated using AlphaFold 2.0 (48,49), where the top-ranked structures were analyzed based on confidence scores and predicted Local Distance Difference Test (pLDDT) scores. RMSD values were computed by superposing (using the superpose module of CCP4) the modeled structures onto the WT (PDB: 7TLY) (50), and statistical significance was assessed using Student's *t*-test. These integrative ML approaches offer a robust framework for predicting sotrovimab resistance mutations and optimizing therapeutic strategies against emerging SARS-CoV-2 variants.

Hybrid QM/MM approach to compute the binding affinity between S-protein RBD and sotrovimab

The starting structure for QM/MM simulations was obtained from RCSB PDB (PDB: 7TLY). Mutant proteins were generated using Pymol with side-chain orientation of mutant residue from the backbone-dependent rotamer library. Rotamer selection was based on executive RMSD and minimum strain concerning the proximal environment. The QM region in each simulation comprised the side chain of the centered amino acid Glu340 (E340) and Tyr508 (Y508), along with side chains of interacting residue within a 4 Å distance. To compare the free energy of the mutant, a set of residues was kept constant in each system. The common residues' side chains within the QM of the E340 system included Ser31, Gly103, Phe105, Phe106, Leu110, Leu335, and Phe338, and the mutational position contains Lys, Ala, Val, Asp, Glu, and Gln residues. Y508 systems comprised side chains of Val104, Gly404, Val107, Asn437, and Pro507. It included Asn, Asp, Cys, His, Phe, and Ser residues in the mutational positions. The partitioning between QM and MM region was chosen to place between Cα-Cβ atoms. The truncated bond was saturated with a dummy link atom. MM partitioning accounted for the remaining system to be described using the Amber ff14SB and GLYCAM force field (51). The MM section is considered in these calculations as point charges (52). The strategic partitioning of QM and MM regions offers an effective framework for accurately capturing the electronic structure surrounding locally the mutant residue. This method highlights critical interactions, such as hydrogen bonding and π-π stacking. Additionally, changes in energetics are fundamental to understanding the resistance mechanism, as they distinctly reflected through the protein mutants. The reliability of QM over MM is well documented for pharmaceutical systems (53). For the geometry optimization, all atoms in the QM region and side chains of residues that are within 8 Å distance of the centered amino acid in the MM region were relaxed. The backbone atoms of the protein were fixed to their starting coordinate positions. Geometry optimization was performed at B3LYP/cc-pVDZ//Amber level of theory. RIJCOSX approximation was used through the resolution of identity for Coulomb (RI-J) and chain of sphere algorithm and exchange integrals (X, RIJCOSX approximation) (54). Grimme's D3BJ damping variant was used for dispersion correction (55). The QM/MM calculations were subsequently performed in Tcl-based Chemshell v3.7.0 (56). The MM calculations were handled through the DL_POLY interface. The quantum chemical calculations were performed using Orca v5.0.2 containing essential engine SHARK for evaluating Fock matrices and integral transformation (57).

Assessing the structural dynamics and biophysical behavior of affinity-modulating designs using coarse-grained and all-atom MD simulations

To complement our integrated computational framework, we analyzed three sotrovimab-S-protein-RBD complexes: 1) WT (PDB: 7TLY) as a control, 2) E340G (a clinically relevant resistance mutation with reduced binding affinity with sotrovimab), and 3) L441W (a designed mutation predicted to enhance the binding affinity toward sotrovimab).

Coarse-grained MD simulations

Coarse-grained MD simulations enabled long-timescale conformational analysis at reduced computational cost (58). Atomistic structures were converted into their corresponding coarse-grained representations using Martinize3, and system preparation involved solvation and ion addition via "insane.py" (59). After energy minimization (50,000 steps of steepest descent), equilibration (50 ns, isothermal-isobaric NPT ensemble) was performed with periodic boundary conditions. Temperature coupling was maintained using Berendsen thermostat (60,61) and Parrinello-Rahman barostat (62) regulated pressure at 1.0 bar. Production simulations ran for 5 μs per system, capturing the structural and conformational transitions.

All-atom MD simulations

All-atom MD simulations were subsequently used to capture the finer molecular details governing sotrovimab binding to the WT and mutant SARS-CoV-2 RBDs. The atomistic resolution allowed for explicit modeling of key interactions, including those mediated by the glycan at N343, which plays a crucial role in antibody recognition and immune evasion (63). All three systems were embedded in a fully solvated environment using the CHARMM-GUI Solution Builder, ensuring precise system parameterization, particularly for the N343 glycan, which was incorporated using predefined CHARMM-GUI glycosylation templates (64). The CHARMM36m force field described both protein and glycan components, accurately modeling carbohydrate-antibody interactions (65). Each system was solvated in a rectangular water box with a 1.0-nm buffer to prevent periodic boundary artifacts, and physiological conditions were maintained with 150 mM KCl. After energy minimization via the steepest descent algorithm, a two-step equilibration was performed: 1) an NVT phase at 303.15 K with restrained heavy atoms to preserve structural integrity and 2) an NPT phase at 1 bar using the Parrinello-Rahman barostat. The LINCS algorithm (66) constrained hydrogen bonds for numerical stability. Production simulations ran for 500 ns with a 2-fs timestep, employing PME (67) for long-range electrostatics (1.2-nm cutoff) and a force-switch modifier for van der Waals interactions. Temperature control was maintained via the V-rescale thermostat with distinct coupling for the protein-glycan complex and solvent, whereas the C-rescale barostat regulated isotropic pressure at 1 bar.

Trajectory analysis of coarse-grained and all-atom MD simulations

Analysis of both coarse-grained and all-atom MD simulation trajectories provided insights into structural stability, molecular flexibility, and binding energetics of the sotrovimab-S-protein-RBD complexes. RMSD measured overall stability, root-mean-square-fluctuation (RMSF) highlighted residue-level flexibility within antibody-contact regions, and Rg assessed global compactness. Principal component analysis (PCA) identified dominant conformational motions, correlating with simulation-derived free energy landscapes (68). The covariance matrix of atomic fluctuations was computed from the trajectory using "gmx_covar", followed by the calculation of eigenvalues and eigenvectors using "gmx_anaeig" to extract the principal components and their associated motions for each system. The free energy landscapes were subsequently constructed to depict energetically favored states as a function of the principal components, and 3D contour plots of these landscapes were generated. The integration of coarse-grained and all-atom MD simulations captured key conformational transitions alongside atomic-level glycan-mediated interactions, offering a comprehensive view of affinity-modulating mechanisms.

End-state binding free energy calculation

The end-state binding free energies of the sotrovimab-S-protein-RBD complexes were computed from the final 250 ns of stable all-atom MD trajectories using gmx_MMPBSA (69), which integrates the MMPBSA.py script from the Amber package. The computational environment was set up with Python3, Miniconda, and required dependencies in a dedicated Conda environment. Key input files included the trajectory file (.xtc), topology (.top, .tpr, .gro), structure (.pdb), and an index file (.ndx) defining the S-protein-RBD and sotrovimab heavy chain as separate groups. The ff14SB force field was applied, ensuring consistency in energy calculations. To assess residue-level contributions to binding affinity, per-residue free energy calculations were performed using gmx_MMPBSA_ana, focusing on residues within 6 Å of the interface. This analysis quantified stabilizing and destabilizing interactions across all three systems, offering insights into the energetic determinants of antibody binding.

Intermolecular interactions between the S-protein RBD and sotrovimab

To assess the impact of mutations on binding affinity, we quantified hydrogen bond occupancy, salt bridge formation, and van der Waals interactions from the all-atom MD simulation trajectories of the three systems using GetContacts (70), identifying key stabilizing interactions disrupted or enhanced by the E340G and L441W mutations (affinity-reducing and affinity-enhancing designs, respectively). The gmx mindist tool in GROMACS (71,72) was utilized to compute the minimum distance and contact frequency within 4 Å between the SARS-CoV-2 S-protein RBD and sotrovimab's heavy chain in coarse-grained MD simulations, offering quantitative insights into interaction persistence and structural proximity. For a detailed energetic evaluation, PPCheck was used to analyze multiple interaction types, including hydrogen bonding, electrostatics, van der Waals forces, and overall stabilizing energy for the WT and affinity-modulating designs (73). This assessment considered residue contacts, short-range interactions, hydrophobic contributions, and salt bridge formations, offering a comprehensive view of binding strength between sotrovimab's heavy chain-S-protein-RBD and sotrovimab's light chain-S-protein-RBD. To further evaluate the intermolecular interactions between the top-ranked affinity-enhancing and affinity-reducing designs of sotrovimab-bound S-protein, we utilized PIMA (74). Multiple energy types and interactions were analyzed, where the total number of interactions obtained provided insights into the nature and strength of the interactions between the S-protein-RBD-sotrovimab's heavy chain and S-protein-RBD-sotrovimab's light chain. Additionally, to explore glycan-mediated interactions, MOE (2022.03) was used to investigate the role of the N343-linked glycan in stabilizing the sotrovimab-RBD interface. Here, the structural snapshots were derived from stable all-atom MD simulation trajectories of WT, affinity-reducing, and affinity-enhancing designs and used subsequently for visualizing and analyzing the glycan-interaction residues.

Validation of the design protocol and comparison with clinical sequences and experimental evidence

To validate our framework, we assessed the concordance between the predicted resistance mutations and SARS-CoV-2 S-protein sequences from COVID-19 patients. We compared mutations generated through our ResScan-design protocol with sequences from the Global Initiative on Sharing All Influenza Data (GISAID) (75). By analyzing mutation frequencies in the sotrovimab-binding site, we evaluated the predictive accuracy of our approach. Further, we examined predicted resistance mutations at two key hotspot residues—E340 (interface) and Y508 (distal site)—against experimentally documented sotrovimab-resistant mutations. To quantify resistance, we computed dAffinity/ΔQM/MM energies for these residues using three different methods, classifying them as resistant or nonresistant. Mutations consistently identified as resistant by at least two methods were compared with reported E340 and Y508 mutations in GISAID. This systematic validation ensured the robustness of our approach in predicting resistance mutations and their impact on binding affinities.

RESULTS

Analysis of interface and selection of sotrovimab-interacting residues for designing

The x-ray crystallographic examination of the SARS-CoV-2 S-protein-RBD complexed with sotrovimab provided valuable insights into the specific amino acids involved in the interaction between the protein chains as well as interaction between N343-linked glycan with sotrovimab (Fig. 1 *A–C*). Through this analysis, we identified a total of 136 sotrovimab-interacting residues within the S-protein-RBD complex that served as potential targets for further investigation (Table 1). Subsequently, we selectively sampled and designed these specific residues with SNPs to evaluate the emergence of potential resistance mutations.

Identification of resistance mutations using ResScan-design protocol

We employed our ResScan-design protocol to design the 136 sotrovimab-interacting residues within the SARS-CoV-2 S-protein RBD. To identify potential resistance hotspots, we compiled a list of SNPs specific to these residues, mimicking natural variations that may arise during viral evolution. To evaluate the impact of mutations on sotrovimab binding, we calculated the relative binding affinity (dAffinity) of each design compared with the WT S-protein-RBD-sotrovimab complex. Our analysis revealed dAffinity values ranging from −6.60 to 5.73 kcal/mol, where positive values indicate reduced binding affinity. The most significant reductions were observed for E340G

TABLE 1 Sotrovimab-interacting residues of the SARS-CoV-2 S-protein-RBD. Each interacting residue was designed with a minimal number of residues to mimic the naturally evolving mutations in the S-protein-RBD

SN	Residues	Sampled SNPs	SN	Residues	Sampled SNPs	SN	Residues	Sampled SNPs	SN	Residues	Sampled SNPs
1	Ile332	RNLKMFSTV	36	Pro373	ARQHLST	71	Ile434	RNLKMFSTV	106	Leu492	RQHIMFPSWV
2	Asn334	DHIKSTY	37	Phe374	CILSYV	72	Ala435	DEGPSTV	107	Arg493	NCQGHILKMPSTW
3	Leu335	RQHIMFPSWV	38	Phe377	CILSYV	73	Trp436	RCGLS	108	Ser494	ACLFPTWY
4	Cys336	RGFSWY	39	Val382	ADEGILMF	74	Asn437	DHIKSTY	109	Tyr495	NDCHFS
5	Pro337	ARQHLST	40	Pro384	ARQHLST	75	Ser438	ACLFPTWY	110	Ser496	ACLFPTWY
6	Phe338	CILSYV	41	Leu387	RQHIMFPSWV	76	Asn439	DHIKSTY	111	Phe497	CILSYV
7	Asp339	ANEGHYV	42	Asn388	DHIKSTY	77	Leu441	RQHIMFPSWV	112	Arg498	NCQGHILKMPSTW
8	Glu340	ADQGKV	43	Leu390	RQHIMFPSWV	78	Asp442	ANEGHYV	113	Pro499	ARQHLST
9	Val341	ADEGILMF	44	Cys391	RGFSWY	79	Ser443	ACLFPTWY	114	Val503	ADEGILMF
10	Phe342	CILSYV	45	Phe392	CILSYV	80	Lys444	RNQEIMT	115	Gly504	ARDCESWV
11	Ala344	DEGPSTV	46	Thr393	ARNIKMPS	81	Val445	ADEGILMF	116	His505	RNDQLPY
12	Thr345	ARNIKMPS	47	Asn394	DHIKSTY	82	Ser446	ACLFPTWY	117	Gln506	REHLKP
13	Arg346	NCQGHILKMPSTW	48	Val395	ADEGILMF	83	Gly447	ARDCESWV	118	Pro507	ARQHLST
14	Phe347	CILSYV	49	Tyr396	NDCHFS	84	Asn448	DHIKSTY	119	Tyr508	NDCHFS
15	Ala348	DEGPSTV	50	Ala397	DEGPSTV	85	Tyr449	NDCHFS	120	Arg509	NCQGHILKMPSTW
16	Ser349	ACLFPTWY	51	Asp398	ANEGHYV	86	Asn450	DHIKSTY	121	Val510	ADEGILMF
17	Val350	ADEGILMF	52	Ser399	ACLFPTWY	87	Tyr451	NDCHFS	122	Val511	ADEGILMF
18	Tyr351	NDCHFS	53	Phe400	CILSYV	88	Leu452	RQHIMFPSWV	123	Val512	ADEGILMF
19	Ala352	DEGPSTV	54	Val401	ADEGILMF	89	Tyr453	NDCHFS	124	Leu513	RQHIMFPSWV
20	Trp353	RCGLS	55	Ile402	RNLKMFSTV	90	Arg454	NCQGHILKMPSTW	125	Ser514	ACLFPTWY
21	Asn354	DHIKSTY	56	Arg403	NCQGHILKMPSTW	91	Leu455	RQHIMFPSWV	126	Phe515	CILSYV
22	Arg355	NCQGHILKMPSTW	57	Gly404	ARDCESWV	92	Phe456	CILSYV	127	Glu516	ADQGKV
23	Lys356	RNQEIMT	58	Asp405	ANEGHYV	93	Phe464	CILSYV	128	Leu517	RQHIMFPSWV
24	Arg357	NCQGHILKMPSTW	59	Glu406	ADQGKV	94	Glu465	ADQGKV	129	Leu518	RQHIMFPSWV
25	Ile358	RNLKMFSTV	60	Val407	ADEGILMF	95	Arg466	NCQGHILKMPSTW	130	Ala520	DEGPSTV
26	Ser359	ACLFPTWY	61	Ile410	RNLKMFSTV	96	Asp467	ANEGHYV	131	Pro521	ARQHLST
27	Asn360	DHIKSTY	62	Ile418	RNLKMFSTV	97	Ile468	RNLKMFSTV	132	Ala522	DEGPSTV
28	Cys361	RGFSWY	63	Asn422	DHIKSTY	98	Ser469	ACLFPTWY	133	Thr523	ARNIKMPS
29	Val362	ADEGILMF	64	Tyr423	NDCHFS	99	Thr470	ARNIKMPS	134	Val524	ADEGILMF
30	Ala363	DEGPSTV	65	Leu425	RQHIMFPSWV	100	Glu471	ADQGKV	135	Cys525	RGFSWY
31	Asp364	ANEGHYV	66	Phe429	CILSYV	101	Ile472	RNLKMFSTV	136	Gly526	ARDCESWV
32	Tyr365	NDCHFS	67	Thr430	ARNIKMPS	102	Tyr473	NDCHFS			
33	Leu368	RQHIMFPSWV	68	Gly431	ARDCESWV	103	Tyr489	NDCHFS			
34	Tyr369	NDCHFS	69	Cys432	RGFSWY	104	Phe490	CILSYV			
35	Leu371	RQHIMFPSWV	70	Val433	ADEGILMF	105	Pro491	ARQHLST			

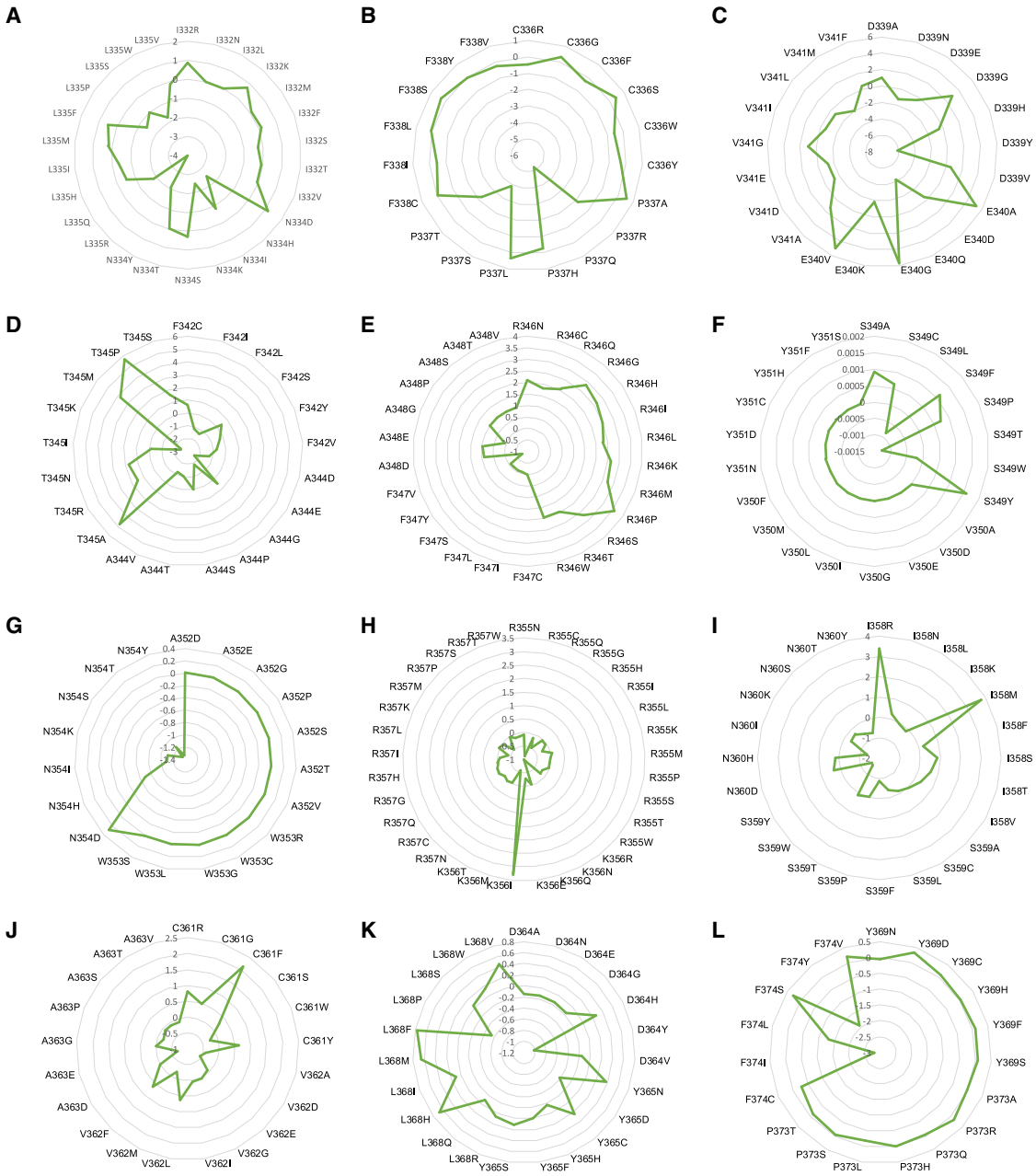

FIGURE 2 The relative binding affinities of all the mutants designed through ResScan-design protocol. Radar plots showing the dAffinity (relative binding affinity) of all the designed mutants computed using the ResScan-design protocol. In each plot (*A–L*) are represented the dAffinity values for all the S-protein-RBD designs that interact with sotrovimab. The dAffinity values of E340 position are provided in Fig. 2 *C*, and the corresponding dAffinity values of all the designs are indicated on the plots.

and T345P, whereas L441W exhibited the lowest dAffinity (Fig. 1 *D–F*). Applying a threshold of 1 kcal/mol, we identified 40 designs with significantly decreased binding affinity, highlighting key hotspot residues such as D339, E340, T345, R346, I358, L441, and R509 as susceptible to immune and drug pressure (Fig. 1 *G*). Among 1191 designed mutants, 621 exhibited positive dAffinity values, suggesting potential resistance development. The Fig. 2 (along with Figs. S1–S3) provide an overview of sotrovimab-interacting residues, their resistance mutations, and corresponding dAffinities.

Rosetta-based design of sotrovimab-S-protein-RBD complex and analysis of physiochemical features

After identifying single-point mutations in the S-protein-RBD that could confer resistance to sotrovimab, we

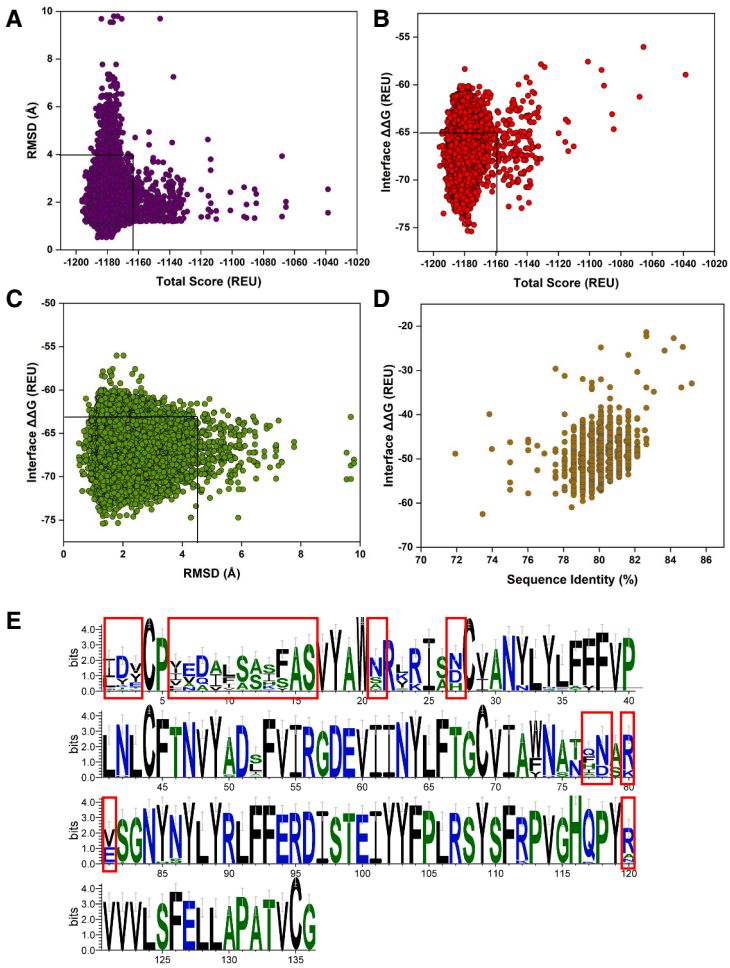

(1) Ile332, (2) Asn334, (3) Leu335, (4) Cys336, (5) Pro337, (6) Phe338, (7) Asp339, (8) Glu340, (9) Val341, (10) Phe342, (11) Ala344, (12) Thr345, (13) Arg346, (14) Phe347, (15) Ala348, (16) Ser349, (17) Val350, (18) Tyr351, (19) Ala352, (20) Trp353, (21) Asn354, (22) Arg355, (23) Lys356, (24) Arg357, (25) Ile358, (26) Ser359, (27) Asn360, (28) Cys361, (29) Val362, (30) Ala363, (31) Asp364, (32) Tyr365, (33) Leu368, (34) Tyr369, (35) Leu371, (36) Pro373, (37) Phe374, (38) Phe377, (39) Val382, (40) Pro384, (41) Leu387, (42) Asn388, (43) Leu390, (44) Cys391, (45) Phe392, (46) Thr393, (47) Asn394, (48) Val395, (49) Tyr396, (50) Ala397, (51) Asp398, (52) Ser399, (53) Phe400, (54) Val401, (55) Ile402, (56) Arg403, (57) Gly404, (58) Asp405, (59) Glu406, (60) Val407, (61) Ile410, (62) Ile418, (63) Asn422, (64) Tyr423, (65) Leu425, (66) Phe429, (67) Thr430, (68) Gly431, (69) Cys432, (70) Val433, (71) Ile434, (72) Ala435, (73) Trp436, (74) Asn437, (75) Ser438, (76) Asp439, (77) Leu441, (78) Asp442, (79) Ser432, (80) Lys444, (81) Val445, (82) Ser446, (83) Gly447, (84) Asn448, (85) Tyr449, (86) Asn450, (87) Tyr451, (88) Leu452, (89) Tyr453, (90) Arg454, (91) Leu455, (92) Phe456, (93) Phe464, (94) Glu465, (95) Arg466, (96) Asp467, (97) Ile468, (98) Ser469, (99) Thr470, (100) Glu471, (101) Ile472, (102) Tyr473, (103) Tyr489, (104) Phe490, (105) Pro491, (106) Leu492, (107) Arg493, (108) Ser494, (109) Tyr495, (110) Ser496, (111) Phe497, (112) Arg498, (113) Pro499, (114) Val503, (115) Gly504, (116) His505, (117) Gln406, (118) Pro507, (119) Tyr508, (120) Arg509, (121) Val510, (122) Val511, (123) Val512, (124) Leu513, (125) Ser514, (126) Phe515, (127) Glu516, (128) Leu517, (129) Leu518, (130) Ala520, (131) Pro521, (132) Ala522, (133) Thr523, (134) Val524, (135) Cys525, (136) Gly526.

FIGURE 3 Rosetta-based interface design of the Sotrovimab-S-protein-RBD complex, associated physicochemical features, and sequence logo of affinity-reducing designs depicting Sotrovimab-interacting S-protein-RBD residue types and frequencies. Physicochemical parameters obtained from the interface-based design of the sotrovimab-S-protein-RBD complex, where (*A*) demonstrates the correlation between Rosetta total score and RMSD (compared with the native structure) for all the 100,000 designs of the sotrovimab-bound S-protein-RDP complex. (*B*) Relationship between Rosetta total score and interface ΔΔG (binding affinity) of the designs between sotrovimab and the S-protein-RBD complex. (*C*) Interface ΔΔG versus RMSD analysis of the designs and (*D*) distribution of designs based on interface ΔΔG and percentage of sequence identity of all the sotrovimab-interacting residues of SARS-CoV-2 S-protein-RBD complex. In panels (*A*)–(*C*), the black lines represent the control values where the sotrovimab-interacting residues of the S-protein-RBD were not designed. (*E*) The sequence logos provide a visual representation of the top 30 affinity-reducing designs. The X-axis corresponds to the index of native S-protein residues, whereas the Y-axis indicates the degree of sequence conservation at each position. The symbol heights reflect the relative occurrence of specific amino acids at those positions. Residues demonstrating a wide array of sequence variations and a relatively higher number of sampled amino acids compared with the native S-protein-RBD are highlighted within the red box. There are notable differences in certain residues between the affinity-reducing and affinity-enhancing designs (shown in Fig. S4), indicating the plausibility of resistance mutations. The lower panel presents the native S-protein residues alongside their respective residue indices.

employed Rosetta-based protein-protein interface design to explore potential hotspot residues beyond these mutations. A total of 136 residues interacting with the heavy and light chains of sotrovimab were selected and mutated to naturally occurring SNPs (Table 1). Only interfacial residues were mutated, whereas others were repacked. We generated 100,000 designs and analyzed their physicochemical properties.

To evaluate the designs, we examined the Rosetta total score versus RMSD. Nearly all designs had RMSDs below 8 Å, with over half below 4 Å, suggesting minimal structural perturbation despite mutational changes (Fig. 3 *A*). A control run involving only repacking helped distinguish affinity-enhancing from affinity-reducing designs, with the latter exhibiting increased RMSDs and unfavorable energetics. Notably, the lowest total score designs had RMSDs below 2 Å, indicating minimal conformational shifts (Fig. 3 *A*). Binding affinities (interface ΔΔG) were analyzed against Rosetta total scores. Affinity-reducing designs showed significantly lower affinities and less favorable total scores compared with affinity-enhancing and control designs (Fig. 3 *B*). RMSD versus interface ΔΔG analysis revealed that several affinity-reducing designs with lower affinities exhibited RMSDs above 4 Å, indicating destabilization due to mutations (Fig. 3 *C*). Some affinity-reducing designs, however, retained RMSDs below 4 Å, suggesting that side-chain rearrangements, rather than large structural shifts, contributed to affinity loss. High RMSD affinity-reducing designs exhibited structural alterations, weakening sotrovimab binding (Fig. 3 *C*). Lastly, we analyzed interface ΔΔG against sequence identity. Despite interactions spanning 136 residues, only a subset emerged as mutational

hotspots (Fig. 3 *D*). The designs maintained ∼72%–85% sequence identity with the WT, and affinity-reducing designs showed slightly lower conservation. This suggests that SARS-CoV-2 can develop resistance through mutations at select hotspot residues under evolutionary and immune/drug pressures (Fig. 3 *D*).

Mutational landscape profiles of sotrovimab-bound S-protein-RBD designs

To better understand the sequence diversity between affinity-enhancing and affinity-reducing designs, we analyzed the top 30 designs from each category. Key differences were observed in residues Asn334, Leu335, Phe338, Asp339, Glu340, Val341, Phe342, Ala344, Thr345, Arg346, Phe347, Asn354, Asn360, Ser399, Leu441, Asp442, Lys444, Val445, and Arg509, which exhibited the highest sequence diversity (Figs. 3 *E* and S4). In contrast, residues Asn354, Arg367, Ser359, Asn360, Val362, Tyr365, Leu371, Pro373, Trp436, Ser438, Asp439, Asp443, Ser446, and Tyr449 showed minimal variations. All other residues remained nearly identical across both categories. Comparing single-point mutants generated by ResScan-design and Rosetta design, we identified several shared mutations in the affinity-reducing category, including I332L, N334D, F338L, D339 V/A, E340A, V341A, T345 A/S, R346S, R357K, S359A, N360D/H, V362I, Y365N, L441Q/I, K444R, N450S, and R509N (Figs. 2 and S1–S4). These mutations significantly decreased sotrovimab binding affinity. Additionally, Rosetta-based design uniquely identified E340D and E340Q as resistance-associated mutations, which were not classified as such by ResScan-design. The observed mutation patterns suggest that specific hotspot residues may undergo selective changes, potentially driving resistance against sotrovimab and related monoclonal antibodies.

Machine learning prediction of binding affinities and sotrovimab resistance mutations

We employed an ML-based approach to predict resistance mutations in the SARS-CoV-2 S-protein against sotrovimab, aiming to enhance our understanding of resistance mechanisms and inform therapeutic strategies. To evaluate the feasibility and speed of these predictions compared with CPD approaches, we tested three algorithms—linear regression, decision tree regression, and XGBoost regression. XGBoost was selected for its superior reliability and accuracy. Our model incorporated diverse features, including 1) native and mutated residues, mutation positions, affinity, stability, and their respective changes from CPD calculations, 2) contact-based features such as ΔG (kcal/mol) and K_d (M) from PRODIGY, and 3) structural-sequential data from public sources. XGBoost regression achieved a high correlation of 0.96 (Fig. 4 *A*), and even when trained solely on sequence information, it maintained a strong correlation of 0.91 (Fig. 4 *B*). Position and stability were identified as key determinants of affinity and model accuracy (Fig. 4 *C*). When analyzing hotspot residues E340 and Y508, our model successfully identified all designed E340 mutations as experimentally validated resistance mutations and Y508H as a clinically known resistance mutation (Fig. 4 *D* and *E*). This strong alignment with experimental and clinical findings underscores the efficacy of our ML approach in predicting sotrovimab resistance mutations.

ML-predicted affinity-enhancing and affinity-reducing designs and structural validation

Following the binding affinity computations, an ML-based method, leveraging interface ΔΔG from CPD, was employed to predict new RBD sequences into affinity-enhancing and affinity-reducing groups. This approach utilized the Rosetta total score or interface ΔΔG as input, predicting mutations at 136 distinct positions and generating diverse RBD sequences. Our multiclass-multioutput classification model revealed that affinity-enhancing RBD designs exhibit higher interface ΔΔG compared with affinity-reducing RBD designs. To validate these predictions, we generated 3D structures of selected designs using AlphaFold v2.0 and assessed structural deviations via backbone RMSD. Affinity-enhancing designs showed lower RMSD values (0.97–1.10 Å) compared with affinity-reducing designs (2.31–2.61 Å), indicating greater structural stability (Fig. 4 *F*). Subsequently, the statistical significance of the RMSD values between the affinity-enhancing and affinity-reducing designs was assessed via two-tailed *t*-test, which depicted the *t*-value to be 49.74386, the *p*-value to be <0.00001, and it is significant at $p < 0.05$. Additionally, per-residue pLDDT scores above 90 affirmed the high accuracy of the predicted models. These results highlight the robustness of our ML-based approach in designing RBD sequences with altered binding affinity for sotrovimab.

Interaction details and energetic evaluation using hybrid QM/MM

The hybrid QM/MM approach provides detailed insights into how mutations impact residue interactions and stability within the binding interface. In the E340 system, the QM region plays a crucial role in resistance, with all E340 mutants showing reduced stability compared with WT (Fig. 5 *E*). Structural analysis revealed that A104, W105, and F106 interacted with Glu340 within 2.7–3.0 Å (Fig. 6 *A*; Table 2). Among the mutants, E340G and E340A exhibited the lowest stability, likely due to their smaller side chains, though they maintained key interactions with N334, T345, D339, and K356 from RBD and Y100, E108, S109, and I111 from sotrovimab (Fig. 6 *B* and *D*; Table 2). These findings align with CPD and ML predictions, confirming Gly (G) and

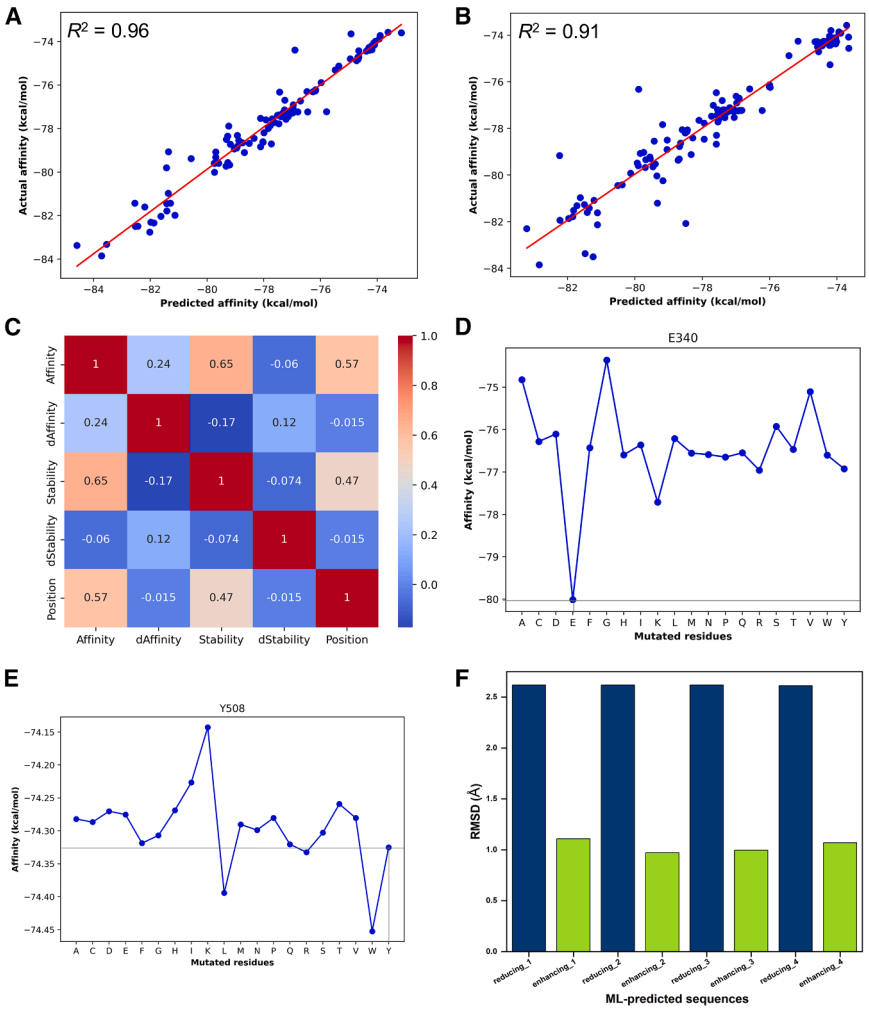

FIGURE 4 Machine-learning-based assessment of affinity correlation, computed physiochemical features, and resistance mutations. (*A*) Comparison of actual affinity values to predicted affinity values using all features used in the XGBoost regressor. (*B*) Comparison of actual affinity values to predicted affinity values for minimal feature sets. In both (*A* and *B*), the X-axis displays the predicted affinity values generated by the XGBoost model, whereas the Y-axis represents the corresponding actual affinity values from CPD. (*C*) Heatmap showing the effect and contribution of all the features on the affinity of the sotrovimab-S-protein-RBD complex. (*D* and *E*) The computed binding affinity of all the mutated residues of E340 and Y508 obtained from the XGBoost regressor model, where the X-axis indicates the mutated residues, and the Y-axis displays the binding affinity values of all mutants. Peaks demonstrating the affinity values above the native position (*denoted using black lines*) indicate the mutants potentially associated with sotrovimab resistance since they have reduced binding affinity. (*F*) Computed backbone RMSDs between the AlphaFold modeled top-ranked structures of the ML-predicted affinity-enhancing and affinity-reducing RBD sequences bound to sotrovimab with the wild-type structure are shown. A two-tailed t-test revealed a highly significant difference at $p < 0.05$ ($t = 49.74386$, $p < 0.00001$) in RMSD values between affinity-enhancing and affinity-reducing designs.

Ala (A) at position 340 as resistance-associated mutations (Fig. 5 *A* and *C*). E340V, in contrast, maintained stability, highlighting the importance of side-chain length in governing sotrovimab-RBD interactions (Fig. 6 *F*). Although E340D, E340K, and E340Q showed similar energetic stability, CPD failed to predict resistance for these mutants, unlike QM/MM and ML (Fig. 6 *C*, *E*, and *G*). Notably, the glycan region of the protein system is included in the MM region and is described as classical point charges in the overall simulations. Their contribution to the energetics is accounted through the Coulombic field on the QM region. Considering our QM region of interest, the glycan regions are located distant, and hence their polarization effect to the QM region is not significant.

For Y508, located near the receptor-binding motif but away from the interface (Fig. 6 *H*), interactions with P373, I402, and N437 were observed within 2.0–2.2 Å (Table S1). Stability analysis showed Y508S as the least stable and Y508C as the most stable mutant (Figs. 5 *F*, 6 *I*, and *N*; Table S1). Other Y508 mutants (D/F/H/N) exhibited comparable stability (Figs. 5 *F* and 6 *J*–*M*; Table S1). Notably, Y508H, a clinically confirmed resistance mutation, aligned well with QM/MM, CPD, and ML predictions, reinforcing the model's accuracy (Fig. 5 *B*–*F*). The QM/MM findings further validated the resistance trend observed across different computational approaches.

Biophysical mechanisms and molecular insights underlying affinity modulation in sotrovimab-RBD interactions

To elucidate the biophysical, structural, and energetic determinants of sotrovimab binding to the SARS-CoV-2 S-protein-RBD, we performed extensive multiscale simulations and interaction analysis. Coarse-grained MD simulations revealed significant instability in the affinity-reducing design (RMSD 1.02 nm), contrasting with the stable WT and affinity-enhancing systems (RMSD 0.26 nm each) (Fig. 7 *A*). Similarly, average RMSF profiles of coarse-grained WT, affinity-enhancing, and affinity-reducing designs for the RBD were found to be 0.12 nm, 0.11 nm, and 0.13 nm, respectively (Fig. 7 *B*). All-atom MD corroborated

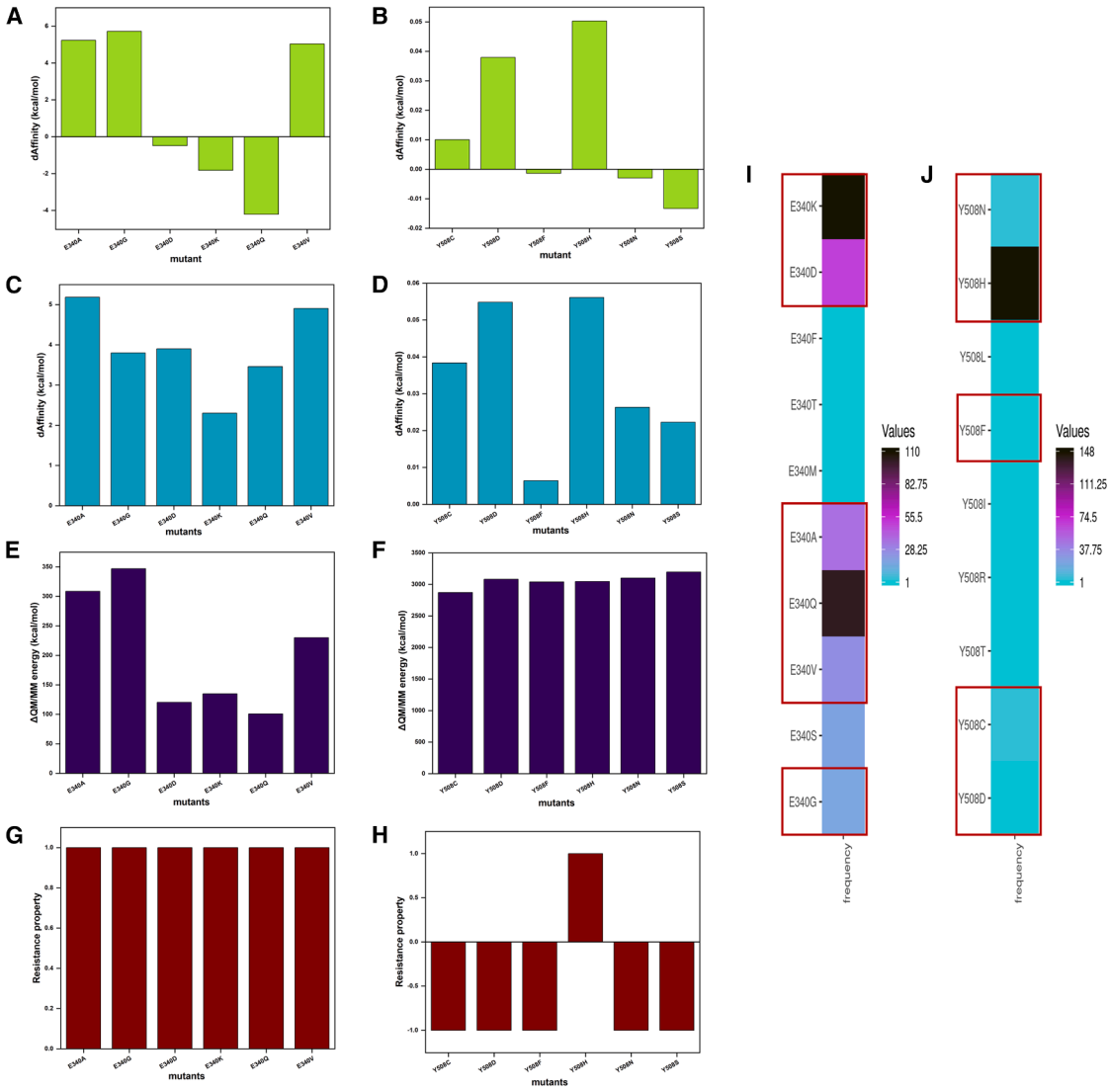

FIGURE 5 Comparative analysis and prediction of resistance mutations as determined using the integrated framework. (*A*) and (*B*) showcase the dAffinity values of the E340 and Y508 mutants utilizing CPD. (*C*) and (*D*) represent the computed dAffinities utilizing the XGBoost machine learning algorithm. In (*A*)–(*D*), Y-axis indicates the dAffinity scores, and X-axis highlights the respective mutants. (*E*) and (*F*) depict the ΔQM/MM energies of the mutants computed from the QM/MM approach, where the Y-axis represents the relative QM/MM energy, and the X-axis highlights the mutants. (*G*) and (*H*) show the mutants exhibiting resistance to sotrovimab as determined from the experimental findings (after sotrovimab treatment). The Y-axis represents the resistance property corresponding to each mutant, whereas the mutant identity is given on the X-axis. The "+1" value on the Y-axis indicates the mutations that are clinically reported and experimentally shown to be resistance to sotrovimab. (*I*) and (*J*) show heatmaps of all the clinically known mutations and their frequency for E340 and Y508 residues as retrieved from GISAID. The sotrovimab resistance mutations as predicted from our framework are shown within red boxes, which show a 60% and 55.5% concurrence with the clinically reported mutations for E340 and Y508, respectively.

these findings, showing the affinity-enhancing design with the lowest RMSD (0.35 nm) and backbone fluctuations (RMSF 0.16 nm), indicating enhanced stability (Fig. 7 *G* and *H*). Conversely, the affinity-reducing design exhibited the highest RMSD (0.41 nm) and RMSF (0.21 nm), reflecting increased flexibility (Fig. 7 *G* and *H*). The WT exhibited an average RMSD of 0.39 nm and average RMSF of 0.18 nm for the RBD region (Fig. 7 *G* and *H*). Although coarse-grained MD showed comparable Rg across all systems (2.42 for WT, 2.41 nm for affinity-enhancing and 2.40 nm for affinity-reducing designs), all-atom MD revealed a slightly expanded but stable conformation for the affinity-enhancing design (1.89 nm) compared with affinity-reducing and WT (1.85 nm each), highlighting the favorable structural properties of affinity-enhancing design for sotrovimab binding (Fig. 7 *C* and *I*).

The PCA and free energy landscape (FEL) analysis further underscored these trends, with the affinity-enhancing and WT complexes occupying lower-energy states and the affinity-reducing design exhibiting a high-energy conformational landscape. PCA identified dominant collective motions in the WT and affinity-modulating

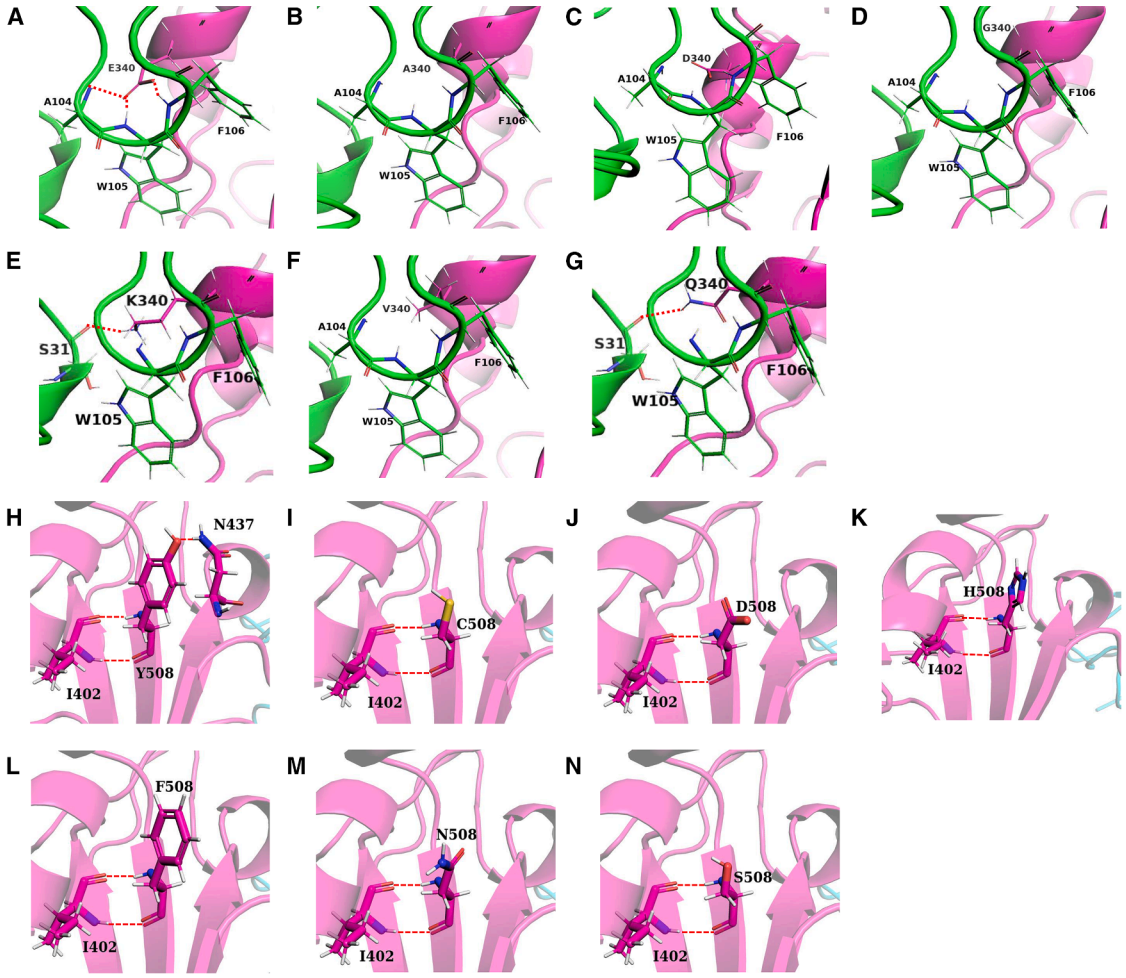

FIGURE 6 Intermolecular and intramolecular interactions obtained from the QM/MM-generated structures of E340 and Y508 wild-type and mutants bound to sotrovimab. The intermolecular interactions obtained from the QM/MM derived structures of E340 system bound to sotrovimab is shown. Here, the S-protein RBD is depicted in magenta, whereas the heavy chain of sotrovimab is shown in green. The polar contacts between residues of the RBD and the heavy chain of sotrovimab are shown in red dotted lines, indicating potential hydrogen bonding interactions. Specifically, (*A*) shows interactions of wild-type E340 and (*B*)–(*G*) show interactions of E340A, E340D, E340G, E340K, E340V, and the E340Q mutants, respectively. Next, the intramolecular interactions of Y508 system are shown. Here, the polar contacts are highlighted in red dotted lines, indicating potential hydrogen bonding interactions. (*H*) shows the intramolecular interactions occurred within the wild-type Y508, whereas (*I*)–(*N*) show the intramolecular interactions of Y508C, Y508D, Y508H, Y508F, Y508N, and Y508S mutants, respectively. In (*H*)–(*N*), the S-protein-RBD is shown in magenta cartoon.

designs, with FEL analysis quantifying their energetic preferences. The first two eigenvectors accounted for most motions, with covariance matrix analysis showing higher trace values for the affinity-reducing design (233.45 nm^2) compared with the WT (26.67 nm^2) and affinity-enhancing variant (25.42 nm^2) in the coarse-grained MD simulations (Fig. 7 *D–F*), indicating increased flexibility and instability. FEL results confirmed that the affinity-enhancing and WT variants occupied lower-energy states, whereas the affinity-reducing design exhibited a more expanded, high-energy landscape. All-atom MD-based PCA further supported these observations, with the affinity-reducing design displaying the highest trace value (391.10 nm^2), followed by the WT (311.43 nm^2) and the affinity-enhancing design (268.51 nm^2), reinforcing the stability-enhancing effects of the affinity-enhancing mutation and the destabilizing impact of the affinity-reducing mutation (Fig. 7 *J–L*).

End-state binding free energies (MM/PBSA) were computed over the final 250-ns all-atom MD simulations, revealing binding affinities of −58.59 kcal/mol (WT), −52.42 kcal/mol (affinity-reducing), and −59.46 kcal/mol (affinity-enhancing) (Table 3). Energy decomposition highlighted the contributions of van der Waals, electrostatic, and solvation energies, with key residues Trp105 and Phe106 enhancing binding in the WT and affinity-enhancing complexes, whereas residue Tyr100 played a significant role in the affinity-reducing design (Fig. 7 *M–O*). Notably, Leu110 contributed substantially to the enhanced binding affinity in the affinity-enhancing design (Fig. 7 *M–O*). These findings highlight the critical role of specific residue interactions in modulating the sotrovimab-S-protein-RBD binding

TABLE 2 Summary of interactions between SARS-CoV-2 RBD and heavy chain of sotrovimab at the residue level for the E340 system

	RBD		Heavy chain		
System	Residue	Atom name	Residue	Atom name	Distance range (Å)
E340	Asn334	OD1 (donor)	Thr30	OG1 (acceptor)	2.73–2.92
E340A					
E340G					
E340K					
E340Q					
E340V (All System)					
Except E340K	Asp339	OD2 (donor)	Tyr100	OH (acceptor)	2.60–2.69
All System	Asn343	ND2 (acceptor)	Tyr100	OH (donor)	2.68–2.94
Except E340A	Asn343	O (donor)	Ile111	N (acceptor)	3.14
All System	Thr345	OG1 (acceptor)	Ser109	O (donor)	3.28–3.30
Except E340V	Thr345	N (acceptor)	Ser109	O (donor)	3.19
All System	Lys356	NZ (acceptor)	Glu108	OE1 (donor)	2.60–2.72
Interaction contributed by the wild-type and mutated residues					
E340	Glu340	OE1 (donor)	Ala104	N (acceptor)	2.70
	Glu340	OE2 (donor)	Phe106	N (acceptor)	3.00
	Glu340	OE1 (donor)	Trp105	N (acceptor)	2.92
E340K	Lys340	NZ (acceptor)	Ser31	O (donor)	2.92
E340Q	Gln340	HE21 (acceptor)	Ser31	O (donor)	3.08

It presents information on wild-type and mutated residues, their respective atoms in RBD, the interacting residues and atoms in the heavy chain of sotrovimab, and the distance range of the bonds formed.

affinity across different complexes. In Fig. 7 *M–O*, the standard deviations are represented by solin lines within the bars.

Intermolecular interactions between the S-protein-RBD and sotrovimab

Hydrogen bond analysis revealed fewer interactions in the affinity-reducing design (eight bonds) compared with the WT (14 bonds) and affinity-enhancing design (13 bonds). The resistance mutation E340G disrupted interactions at position 340 with Ala104, Trp105, Phe106 and Gly107, weakening the binding. This finding is consistent with the results from the QM/MM analysis, which also revealed the absence of interactions between G340 and sotrovimab (Fig. 8 *A*). Additionally, both mutations introduced a new bond between Tyr32 and Asp339, while also losing two hydrogen bonds between Tyr32 and AFUC, and Gly113 and AFUC. The van der Waals contacts followed a similar trend, with fewer interactions in the affinity-reducing design (17) compared with the WT and affinity-enhancing design (24 each) (Fig. 8 *B*). However, though G340 in the affinity-reducing design made van der Waals interactions with two other residues, seven interactions were also disrupted at position 340 in the affinity-reducing design, which were retained in the other two systems (Fig. 8 *B*). Contact map analysis from the coarse-grained MD simulations confirmed these findings, with shorter average contact distances in the affinity-enhancing variant (0.35 nm) versus the WT (0.37 nm) and affinity-reducing design (0.52 nm), indicating stronger interactions and improved binding stability (Fig. 8 *C*). It is evident that the WT maintained a slightly greater contact distance, indicating moderate flexibility while preserving key interactions. In contrast, the affinity-reducing design exhibited a significantly larger contact distance, implying weakened interactions and potential disruption of critical epitope contacts. Additionally, analysis of contact frequencies revealed that the affinity-reducing design exhibited significantly reduced contact frequency (average 1.46) throughout the coarse-grained MD simulations compared with the WT (average 6.58) and affinity-enhancing design (7.30) (Fig. 8 *D*). These findings highlight how specific mutations modulate sotrovimab binding, with the affinity-enhancing design reinforcing stable interactions, whereas affinity-reducing design promotes structural destabilization, resulting in reduced binding.

A comparative analysis of interaction energy among WT and affinity-modulating designs, including two affinity-enhancing (D339Y, L441W) and two affinity-reducing (E340V, E340G) designs, demonstrated higher stabilizing energy in the affinity-enhancing designs (−184.82 and −211.60 kJ/mol, respectively) compared with the WT (−181.66 kJ/mol) and affinity-reducing designs (−154.18 and −151.59 kJ/mol, respectively). The affinity-reducing designs predominantly exhibited weaker van der Waals interactions, whereas the affinity-enhancing designs formed stronger hydrogen bonds and electrostatic interactions (Table S2). The heavy chain exhibited significant energy variations, highlighting its role in binding affinity modulation. These results underscore the destabilizing effects of affinity-reducing mutations on sotrovimab-RBD interactions,

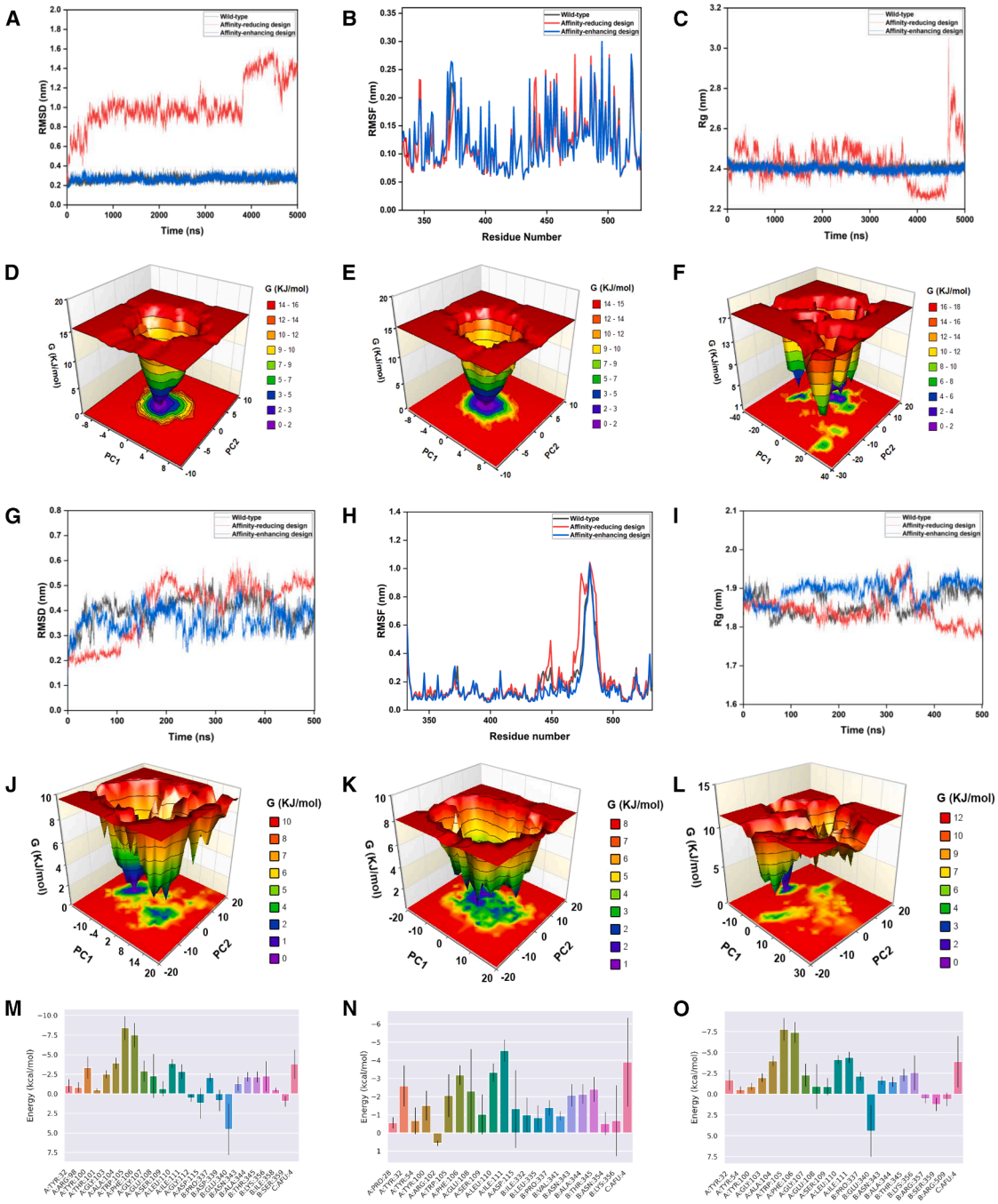

FIGURE 7 Comparative analysis of physicochemical properties, structural dynamics, Gibbs free energy landscapes (FELs), and per-residue binding energy for sotrovimab-S-protein-RBD complexes across wild-type, affinity-reducing, and affinity-enhancing designs during coarse-grained and all-atom MD simulations. (*A*) Backbone RMSD profiles from coarse-grained MD simulations, reflecting overall structural stability. (*B*) RMSF profiles highlighting residue-specific fluctuations in the RBD over 5-μs coarse-grained MD simulations. (*C*) Radius of gyration (Rg) profiles indicating structural compactness of sotrovimab-S-protein-RBD complexes. (*D–F*) 3D FEL contour plots from coarse-grained MD trajectories for wild-type, affinity-enhancing, and affinity-reducing systems, mapped onto the first two principal components. (*G–I*) RMSD, RMSF, and Rg profiles from 500-ns all-atom MD simulations, providing insights into stability, flexibility, and compactness. (*J–L*) 3D FEL contour plots from all-atom MD simulations of wild-type, affinity-enhancing and affinity-reducing designs, mapped onto first two principal components, where red indicates high-energy states, yellow and green represent intermediate states, and blue/purple highlight the most stable, low-energy states. (*M–O*) Comparative per-residue binding energy contributions for (*M*) wild-type, (*N*) affinity-reducing, and (*O*) affinity-enhancing complexes, with bar plots emphasizing key residues contributing to enhanced binding in affinity-enhancing and wild-type complexes. Standard deviations are represented by solid lines within the bars.

TABLE 3 Table showing the end-state binding free energy values between the S-protein-RBD and sotrovimab heavy chain from the stable MD simulation trajectories of the wild-type, affinity-reducing, and affinity-enhancing designs from the all-atom MD simulations

Molecular system	Energy component	Average	SD (prop.)[a]	(SD)[b]	SEM (prop.)[c]	(SEM)[d]
Wild-type	ΔBOND	0	10.25	0	0.65	0
	ΔANGLE	0	16.71	0	1.05	0
	ΔDIHED	0	8.77	0	0.55	0
	ΔUB	0	3.14	0	0.2	0
	ΔIMP	0	3.45	0	0.22	0
	ΔCMAP	0	5.51	0	0.35	0
	ΔVDWAALS	−55.58	8.68	6.08	0.55	0.38
	ΔEEL	−132.96	55.98	24.77	3.53	1.56
	Δ1-4 VDW	0	6.31	0	0.4	0
	Δ1-4 EEL	0	26.7	0	1.69	0
	ΔEPB	137.61	52.58	21.92	3.32	1.38
	ΔENPOLAR	−7.56	0.51	0.5	0.03	0.03
	ΔEDISPER	0	0	0	0	0
	ΔGGAS	−188.53	57.11	25.27	3.6	1.59
	ΔGSOLV	130.05	52.58	21.73	3.32	1.37
	ΔTOTAL	**−58.49**	**77.63**	**11.19**	**4.9**	**0.71**
Affinity-reducing design	ΔBOND	0	10.01	0	0.63	0
	ΔANGLE	0	17.99	0	1.14	0
	ΔDIHED	0	9.1	0	0.57	0
	ΔUB	0	2.96	0	0.19	0
	ΔIMP	0	3.81	0	0.24	0
	ΔCMAP	0	5.12	0	0.32	0
	ΔVDWAALS	−54.25	9.86	6.73	0.62	0.42
	ΔEEL	−103.08	50.24	30.47	3.17	1.92
	Δ1-4 VDW	0	6.51	0	0.41	0
	Δ1-4 EEL	0	29.13	0	1.84	0
	ΔEPB	112.87	33.21	26.37	2.1	1.66
	ΔENPOLAR	−7.96	0.2	0.69	0.01	0.04
	ΔEDISPER	0	0	0	0	0
	ΔGGAS	−157.33	51.68	31.08	3.26	1.96
	ΔGSOLV	104.91	33.21	26.05	2.1	1.64
	ΔTOTAL	**−52.42**	**61.43**	**7.81**	**3.88**	**0.49**
Affinity-enhancing design	ΔBOND	0	11.7	0	0.74	0
	ΔANGLE	0	14.92	0	0.94	0
	ΔDIHED	0	7.41	0	0.47	0
	ΔUB	0	3.24	0	0.2	0
	ΔIMP	0	3.54	0	0.22	0
	ΔCMAP	0	5.13	0	0.32	0
	ΔVDWAALS	−55.17	9.14	6.22	0.58	0.39
	ΔEEL	−157.46	47.44	29.98	2.99	1.89
	Δ1-4 VDW	0	5.91	0	0.37	0
	Δ1-4 EEL	0	25.54	0	1.61	0
	ΔEPB	160.79	37.08	24.94	2.34	1.57
	ΔENPOLAR	−7.62	0.44	0.66	0.03	0.04
	ΔEDISPER	0	0	0	0	0
	ΔGGAS	−212.63	48.82	29.76	3.08	1.88
	ΔGSOLV	153.17	37.09	24.64	2.34	1.56
	ΔTOTAL	**−59.46**	**61.31**	**9.45**	**3.87**	**0.6**

All values are presented in kcal/mol.
[a]The standard deviation (SD) is acquired through the propagation of the uncertainty formula.
[b]SD represents the sample standard deviation.
[c]The standard error of the mean (SEM) is determined through the propagation of the uncertainty formula.
[d]SEM denotes the sample standard error of the mean.

thereby causing resistance against sotrovimab. Further analysis of interface interactions revealed 19 fewer interactions in the affinity-reducing design compared with the affinity-enhancing design, though no changes were observed in the light chain (Tables S3 and S4). Specifically, in the high-affinity design, Arg102, Trp105, and Phe106 established hydrogen bonds with Glu340, whereas Glu108 engaged in electrostatic interactions with Glu340 and Arg346. These findings highlight the pivotal role of hydrogen bonding and electrostatic interactions in modulating sotrovimab's binding efficacy and neutralization potential (Fig. S5).

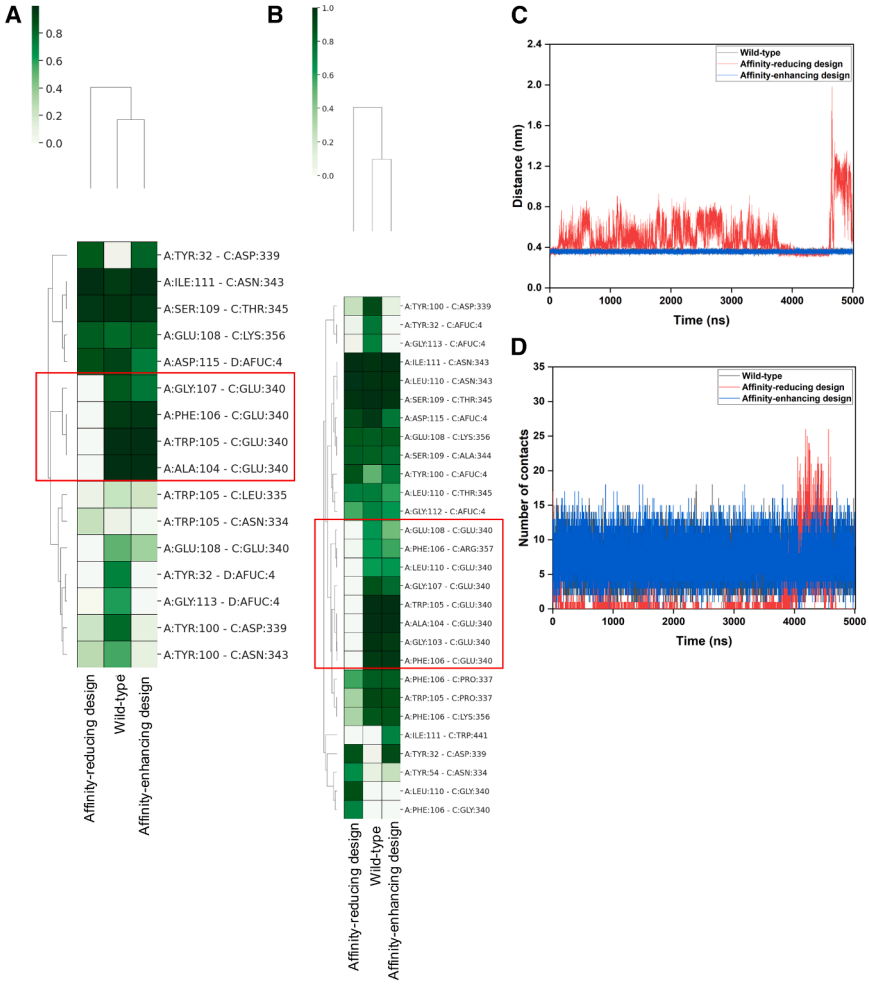

FIGURE 8 Clustograms illustrating interactions between S-protein-RBD and sotrovimab for the wild-type and affinity-modulating designs are shown. (*A*) Hydrogen bond interactions and (*B*) van der Waals interactions are shown across the sotrovimab-S-protein-RBD complexes for wild-type and the affinity-modulating designs. The gradient from white to green represents the increased frequency of interactions over the stable phase of the all-atom MD simulations. In these clustograms, "A" denotes chain A (sotrovimab heavy chain), and "C" denotes chain C (S-protein RBD), and "D" denotes chain D (*N*-343 linked glycan). The red box shows interactions that are prominently varied between affinity-enhancing and affinity-reducing designs. (*C*) Temporal evolution of inter-bead contacts (formed between S-protein-RBD and sotrovimab heavy chain) over a 5000-ns coarse-grained MD simulation for the wild-type and affinity-modulating designs. The Y-axis indicates the distance (nm) between interacting coarse-grained beads, whereas the X-axis represents simulation time (ns). (*D*) Number of contacts formed between S-protein-RBD and sotrovimab heavy chain (within 4Å) over the course of MD simulations for wild-type and the affinity-modulating designs.

Role of N343-linked glycan in sotrovimab-RBD interactions

Finally, we explored the role of N343-linked glycan in modulating sotrovimab-RBD interactions. Analysis of structural snapshots from the stable all-atom MD trajectories revealed that the affinity-enhancing design exhibited the highest number of glycan-mediated interactions (6), involving key residues such as Thr57 (B), Arg98 (A), and Asp339 (C) (Fig. 9 *C*). The WT and affinity-reducing designs each showed four glycan interactions, with the affinity-reducing design exhibiting distinct interaction patterns involving residues like Tyr32 (A) and Asn370 (C) (Fig. 9 *A* and *B*). These findings suggest that glycan interactions contribute to the overall binding stability and affinity of sotrovimab to the RBD, with the affinity-enhancing mutation potentially reinforcing these stabilizing contacts. Here, chains B, A, and C represent the sotrovimab light chain, heavy chain, and SARS-CoV-2 S-protein-RBD, respectively (Fig. 9). Furthermore, in presence of N343 linked glycan, clear differences in the stabilizing interactions and energies were observed between sotrovimab and S-protein-RBD for the WT and affinity-modulating designs (Table 3), indicating the preferential role of glycan in modulating binding affinity and governing resistance. As prior studies have suggested that N343 glycan presence does not significantly enhance sotrovimab binding, it is important to note that it may play a role in immune evasion by reducing accessibility to specific neutralizing epitopes. Overall, though, our results indicated a loss of interactions and binding in the affinity-reducing design, whether an affinity-reducing mutation leads to a complete loss or partial retention of binding depends on the interplay between direct residue interactions and the structural influence of glycans like N343.

Validation of design protocol and correlation with experimental observations

To validate our predictive framework, we first generated mutated designs of the S-protein using ResScan-design and shortlisted mutations within the sotrovimab-binding site. Clinically sequenced mutations from COVID-19 patients were obtained from the GISAID database, along with their frequencies. Among 452 mutations from GISAID, 110

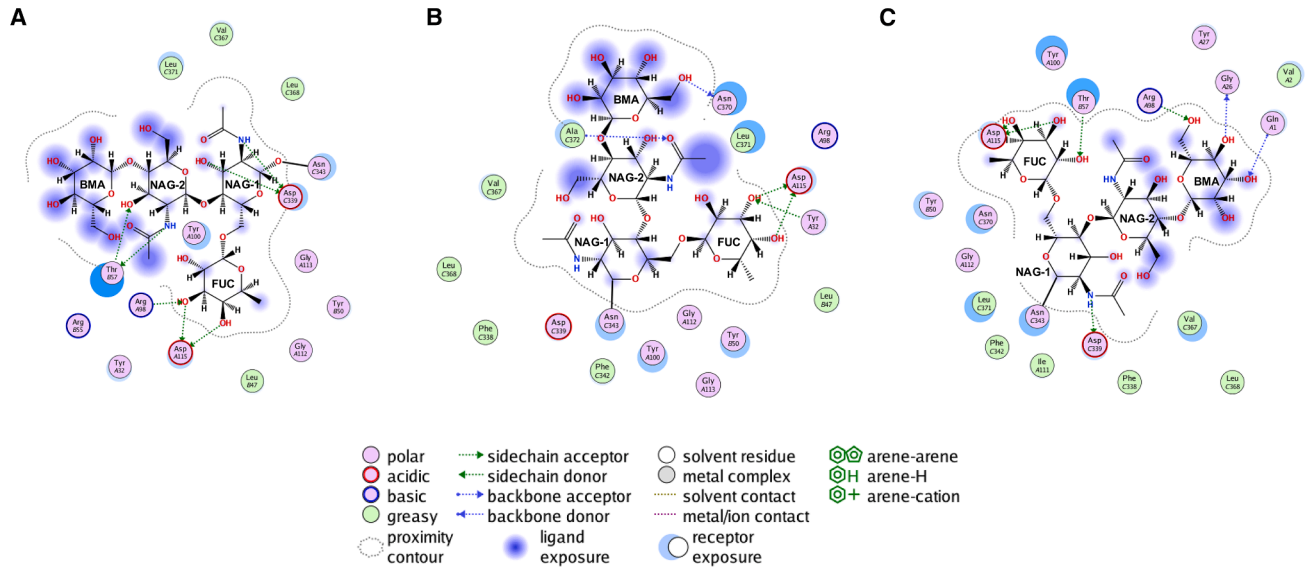

FIGURE 9 Two-dimensional interaction maps showing the interactions of N343-linked glycan in the sotrovimab-S-protein-RBD complexes obtained from the stable all-atom MD simulation trajectories for the wild-type and affinity-modulating designs. (*A*) illustrates interactions of the N343-linked glycan within the sotrovimab-S-protein-RBD complex for the wild-type, whereas (*B*) and (*C*) depict its interactions in affinity-reducing and affinity-enhancing designs, respectively, obtained from the stable all-atom MD simulation trajectories. Here, "A", "B" and "C" shown within the nodes denotes the sotrovimab heavy chain, sotrovimab light chain, and S-protein-RBD, respectively. The types of interactions are shown in the bottom of the figure.

exhibited plausible resistance based on ResScan-design predictions, showing a 24% concurrence with documented clinical mutations (Fig. 10). Notably, the G339 residue in the WT S-protein, which naturally mutated to D339 in the Omicron variant, highlights the selective pressure exerted by antiviral drugs like sotrovimab, driving resistance evolution. However, mutation frequencies in GISAID do not necessarily correlate with calculated affinity values. Next, we validated our framework's predictions—integrating CPD, ML, and hybrid QM/MM simulations—against experimentally reported resistance mutations at E340 and Y508 (Fig. 5 *G* and *H*). Our model accurately identified E340 A/G/D/K/Q/V and Y508H as resistance mutations, aligning with experimental findings, and it additionally predicted Y508C, Y508D, Y508F, Y508N, and Y508S as potential resistance mutations requiring further investigation in sotrovimab-treated patients (Fig. 5). To further assess real-world applicability, we established a benchmark where a mutation qualifies as resistant if its dAffinity/ΔE QM/MM values are positive and consistent across at least two of the three computational methods. Comparing our predicted resistance mutations with GISAID-reported mutations, we found a strong correlation—60% for E340 and 55% for Y508 (Fig. 5 *I* and *J*). This alignment with clinical data reinforces the reliability of our framework while highlighting additional positions and mutations that may contribute to sotrovimab resistance.

DISCUSSION

The emergence of resistance mutations in SARS-CoV-2 poses a significant challenge to the efficacy of existing drugs and mAbs. The continuous evolution of the virus and its ability to develop resistance to therapeutics have underscored the need for a comprehensive understanding of the molecular mechanisms underlying resistance (76). Resistance to antiviral drugs and mAbs is a natural consequence of the adaptive evolution of viruses (77). SARS-CoV-2, like other RNA viruses, possesses high mutation rates due to the error-prone nature of its replication machinery (78). This genetic variability allows the virus to rapidly explore sequence space and acquire mutations that confer resistance to antiviral drugs and antibodies. As a result, the development of resistance has been observed for several antiviral drugs, including remdesivir, favipiravir, and molnupiravir, as well as mAbs such as bebtelovimab and sotrovimab. Sotrovimab, targeting the SARS-CoV-2 S-protein, has shown promising efficacy in the treatment of COVID-19 (3–5,34). However, as with other mAbs, the emergence of resistance poses a significant threat to its long-term effectiveness. Resistance to sotrovimab can arise through various mechanisms, including mutations in the viral S-protein that prevent antibody (27,28) binding or structural changes that alter the conformation of the S-protein.

Our study aims to shed light on the resistance developed by SARS-CoV-2 against sotrovimab and provide insights into the molecular basis of this resistance. Through an integrated multiscale framework combining interface-based CPD, sophisticated ML, hybrid QM/MM simulations, and multiscale simulations, we identified key residues, resistance mutations, as well as biophysical mechanisms involved in the interaction between sotrovimab and the S-protein and causing sotrovimab resistance. Our findings

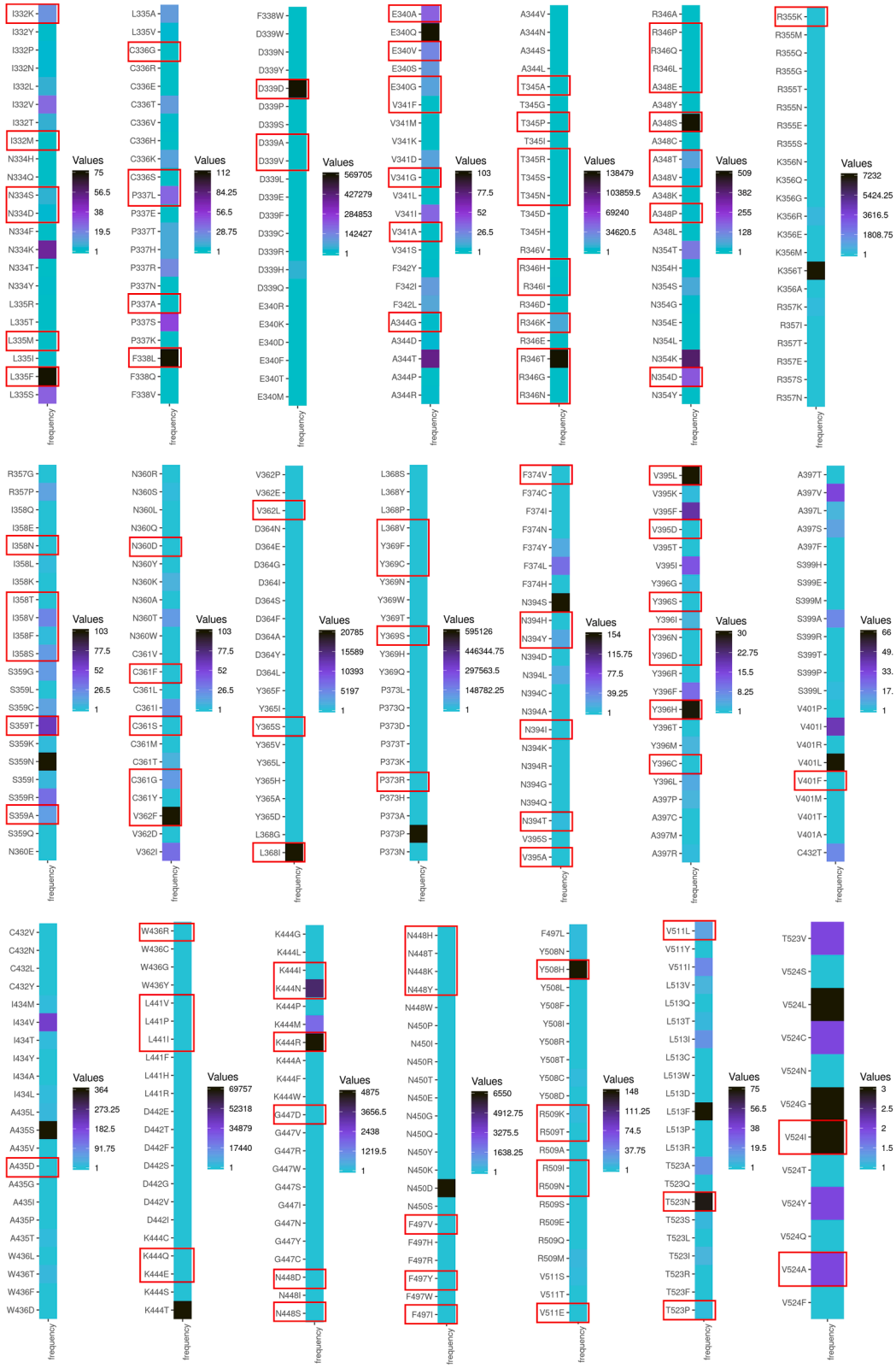

FIGURE 10 Heat maps illustrating the prevalence of S-protein RBD mutations interacting with sotrovimab, using data sourced from GISAID. Mutations identified within the sotrovimab-binding site of the SARS-CoV-2 S-protein, obtained from the GISAID database, are presented. The frequencies of these

(legend continued on next page)

revealed that certain hotspot residues, such as E340 and Y508, are prone to developing resistance mutations against sotrovimab. These mutations can significantly impact the binding affinity between the antibody and the S-protein, ultimately leading to reduced efficacy of sotrovimab in neutralizing the virus. For instance, mutations such as E340G, E340A, and T345P significantly alter the strength and nature of interactions within the sotrovimab-RBD interface. Structural analysis revealed that these mutations disrupt critical hydrogen bonds and van der Waals contacts, thereby reducing binding affinity. For example, E340G and E340A, which replace the negatively charged glutamate with smaller, nonpolar residues, diminish key electrostatic interactions with sotrovimab's heavy chain, destabilizing the complex. Similarly, T345P introduces conformational rigidity that perturbs local backbone flexibility, preventing optimal accommodation of sotrovimab.

Computational modeling further revealed that these resistance mutations induce subtle but functionally significant perturbations in protein conformational landscapes, shifting equilibrium states toward less favorable binding-competent conformations. The energetic analysis demonstrated a redistribution of interaction hotspots, with resistance mutations altering binding free energy contributions from key residues (Fig. 7 *M–O*). Additionally, large-scale conformational sampling indicated that the mutations not only weaken direct protein-protein interactions but also induce allosteric effects that propagate through the RBD, modulating the broader structural framework essential for stable antibody engagement (Fig. 7 *A–F*). Electronic structure calculations confirmed that these alterations extend to local charge distributions, subtly reshaping electrostatic complementarity at the binding interface.

Beyond direct residue-level changes, our analysis also highlights the critical role of glycosylation in modulating these biophysical mechanisms. The glycan at N343 acts as a structural and electrostatic mediator, contributing to the stability of the binding interface. Resistance mutations indirectly alter glycan positioning, affecting its shielding effect and long-range interactions with the antibody (30,79). Changes in glycan dynamics influence the accessibility of key residues, thereby modulating sotrovimab's ability to engage the RBD effectively. Additionally, perturbations in the glycan environment lead to shifts in local electrostatic potential and binding energy landscapes, further exacerbating resistance. These findings underscore how an intricate interplay between point mutations and glycan rearrangements collectively drives sotrovimab escape while highlighting broader implications for antibody design and optimization.

Furthermore, our findings align with and extend previous reports highlighting the role of mutations at E340 and P337 in driving sotrovimab resistance. Prior studies have demonstrated that substitutions at these positions lead to significant reductions in neutralization potency, with mutations such as E340 A/K/Q and P337 L/R/K showing over 50-fold increases in IC_{50} values (16,80,81). In agreement with these observations, our study confirms a notable shift in binding affinity at E340, reinforcing the critical role of this site in sotrovimab escape (Fig. 5 *A*, *C*, and *E*). Although we detect the presence of P337L, the absence of P337R and K356T in our data set suggests potential differences in the prevalence of these mutations across different viral populations or selective pressures exerted during sotrovimab treatment (Fig. 2 *B* and *H*) (82). Additionally, clinical studies have identified a spectrum of resistance mutations in sotrovimab-treated SARS-CoV-2 samples, with several mutations at E340 and P337 emerging as dominant escape variants (81). The association of E340 mutations with the acquisition of a new glycosylation site further suggests that resistance mechanisms may involve not only direct protein-protein interaction disruptions but also glycan-mediated shielding effects that enhance immune evasion (82). Beyond sotrovimab, our findings underscore broader patterns of antibody resistance that parallel those observed for other monoclonal therapies. Resistance to bamlanivimab and etesevimab, for example, is driven by key RBD mutations such as K417N, E484K, and N501Y, which are also implicated in immune escape against multiple therapeutic mAbs (83). Notably, E340K—a mutation identified in our study—has been linked to sotrovimab resistance in multiple reports and shares mechanistic similarities with resistance-conferring mutations affecting cilgavimab (K444 R/E, N450D) and bebtelovimab (V445A) (84). The presence of these recurrent mutations across different antibody classes suggests a degree of convergent evolution, where SARS-CoV-2 selects for substitutions that optimize escape while preserving RBD functionality. The identification of overlapping resistance sites across different mAbs highlights the structural constraints within the RBD that govern antibody escape and suggests that future therapeutic strategies should consider mutational hotspots that facilitate cross-resistance.

Finally, the analysis of the interaction energy within the sotrovimab-S-protein complex provided insights into the contributions of different residues and chains to the binding affinity. Our results highlighted the crucial role of hydrogen bonds and electrostatic interactions in modulating the binding affinity of sotrovimab toward the S-protein RBD. Changes in these interactions, caused by resistance mutations, can result in decreased binding affinity and reduced

mutations obtained from the sequences of SARS-CoV-2-infected COVID-19 patients are indicated by a color gradient ranging from turquoise (low frequency) to black (high frequency). Mutations highlighted within the red boxes represent the designed mutants, suggesting their potential adaptations and resistance to sotrovimab. Our computational analysis showed approximately 24.3% correlation between the designed mutations and currently circulating SARS-CoV-2 S-protein sequences, thereby indicating them as positively selected and resistant toward sotrovimab.

efficacy of the antibody. It is important to note that the development of resistance is a dynamic process influenced by various factors, including viral replication dynamics, host immune responses, and selection pressures from therapeutic interventions. Additionally, the emergence of new variants, such as the Delta and Omicron variants, further complicates the landscape of resistance development. These variants harbor unique mutations in the S-protein, which may confer resistance not only to sotrovimab but also to other mAbs and therapeutics. Ongoing research efforts are focused to address these challenges by developing novel therapeutics that target different epitopes of the S-protein or employ alternative mechanisms to neutralize the virus (85). Combination therapies, using multiple antibodies or a combination of antibodies and antiviral drugs, have also shown promise in mitigating resistance and improving treatment outcomes (86). Our study provides valuable insights into the molecular basis of resistance and highlights the importance of understanding the mutational landscape and structural changes in the S-protein. By employing an integrated framework, we have identified resistance mutations, validated our predictions with clinical and experimental data, and elucidated the key interactions involved in sotrovimab resistance. Our framework demonstrates its potential utility for predicting mutation resistance in other viral diseases and therapeutic targets, presenting new possibilities for personalized and precision medicines. Continued surveillance, research, and innovation are crucial to stay ahead of the evolving virus and effectively control the ongoing COVID-19 pandemic.

Limitations of the study

We acknowledge certain limitations of this work. 1) Although CPD results offers valuable insights into the molecular interactions and binding affinities of the protein-protein complexes, it also has inherent limitations. For instance, due to the complexity of the protein-protein interactions, the large-scale conformational changes may not be fully captured by such computational models, thereby affecting the prediction accuracy. 2) While our study integrates clinical-sequencing data and experimental reports to validate the predicted resistance mutations, it is important to note that experimental validation is still crucial to confirm the functional impact of these mutations. In vitro and in vivo studies are necessary to evaluate the actual binding affinity, neutralizing activity, and therapeutic efficacy of the identified resistance mutations. Despite these limitations, our integrated framework offers a multidimensional approach to predict resistance mutations and enhance our understanding of viral resistance mechanisms.

CONCLUSION

This study introduces an integrated framework utilizing various state-of-the-art computational techniques to identify hotspot residues in the S-protein-RBD of SARS-CoV-2, elucidating potential mutations and resistance against mAbs such as sotrovimab. This multidimensional approach allows us to analyze the binding interface between sotrovimab and the SARS-CoV-2 S-protein, identify key hotspot residues, predict potential resistance mutations relatively quickly, and obtain comprehensive biophysical insights into resistance mechanisms. By correlating our predictions with clinical-sequencing data and experimental reports from sotrovimab-treated patients, we have validated the accuracy and reliability of our framework. Our findings not only align well with known clinical-sequencing resistance mutations but also reveal additional resistance mutations that were previously unidentified. This approach ensures that our findings are relevant and applicable to the actual challenges faced in clinical settings. Furthermore, our study highlights the importance of combining interface-based CPD, ML, hybrid QM/MM, and multiscale MD simulations to unravel resistance mutations and optimize the design of antibody therapeutics. In conclusion, this integrated framework serves as a valuable tool for future research, providing a framework for the development of more effective antibody-based treatments against SARS-CoV-2 variants. Moving forward, the continued investigation of resistance mutations and the optimization of antibody treatments will be crucial in combating the ongoing challenges posed by SARS-CoV-2 and its variants.

DATA AND CODE AVAILABILITY

The data that support the findings of this study are available from the corresponding author (aditya.bce@iitbhu.ac.in) upon reasonable request.

ACKNOWLEDGMENTS

The authors sincerely acknowledge the infrastructure facilities of IIT (BHU) Varanasi and DST-funded I-DAPT Hub Foundation, IIT (BHU) (DST/NMICPS/TIH11/IIT(BHU)2020/02). Further, the computing resources of PARAM Shivay Facility under the National Supercomputing Mission, Government of India at the IIT (BHU), Varanasi, are gratefully acknowledged. A.S. and S.M. acknowledge the Ministry of Human Resource Development (MHRD), the Government of India, and IIT (BHU) for their research fellowships. T.T. acknowledges the support of a project grant from the Indian Council of Medical Research (ICMR) (grant 52/06/2020/BIO/BMS) Government of India, India. R.K.K. thanks ICMR Center for Excellence (grant no. 5/3/8/20/2019-ITR) and SERB, DST (SRG/2022/000858) for funding support. A.K.P. is grateful for the financial support received from ICMR (Dev/SG-04/2024(E-Office 218466) and the Indian Institute of Technology (BHU) Varanasi's Seed Grant ref. No. IIT (BHU)/Budget/19-(14)/2022-23/17507.

AUTHOR CONTRIBUTIONS

A.S., S.M., S.K., T.T., R.K.K., and A.K.P contributed to the formal analysis, investigation, methodology, and writing of the original draft. A.K.P contributed to conceptualization. A.K.P contributed to funding acquisition and project administration. All authors contributed to the writing and preparing the final version of the manuscript.

DECLARATION OF INTERESTS

The authors declare no competing interests.

SUPPORTING MATERIAL

Supporting material can be found online at https://doi.org/10.1016/j.bpj.2025.05.015.

REFERENCES

1. Markov, P. V., M. Ghafari, …, A. Katzourakis. 2023. The evolution of SARS-CoV-2. *Nat. Rev. Microbiol.* 21:361–379.
2. Padhi, A. K., J. Dandapat, …, T. Tripathi. 2021. Interface-based design of the favipiravir-binding site in SARS-CoV-2 RNA-dependent RNA polymerase reveals mutations conferring resistance to chain termination. *FEBS Lett.* 595:2366–2382.
3. Padhi, A. K., R. Shukla, …, T. Tripathi. 2021. High-throughput rational design of the remdesivir binding site in the RdRp of SARS-CoV-2: implications for potential resistance. *iScience.* 24:101992.
4. Kabinger, F., C. Stiller, …, P. Cramer. 2021. Mechanism of molnupiravir-induced SARS-CoV-2 mutagenesis. *Nat. Struct. Mol. Biol.* 28:740–746.
5. Padhi, A. K., and T. Tripathi. 2022. Hotspot residues and resistance mutations in the nirmatrelvir-binding site of SARS-CoV-2 main protease: Design, identification, and correlation with globally circulating viral genomes. *Biochem. Biophys. Res. Commun.* 629:54–60.
6. Choudhary, M. C., K. W. Chew, …, A. Shahkolahi. 2022. Emergence of SARS-CoV-2 escape mutations during Bamlanivimab therapy in a phase II randomized clinical trial. *Nat. Microbiol.* 7:1906–1917.
7. Hwang, Y.-C., R.-M. Lu, …, H.-C. Wu. 2022. Monoclonal antibodies for COVID-19 therapy and SARS-CoV-2 detection. *J. Biomed. Sci.* 29:1.
8. Jackson, C. B., M. Farzan, …, H. Choe. 2022. Mechanisms of SARS-CoV-2 entry into cells. *Nat. Rev. Mol. Cell Biol.* 23:3–20.
9. Gupta, A., Y. Gonzalez-Rojas; …, COMET-ICE Investigators. 2021. Early Treatment for Covid-19 with SARS-CoV-2 Neutralizing Antibody Sotrovimab. *N. Engl. J. Med.* 385:1941–1950.
10. Shapiro, A. E., E. Sarkis, …, A. Kohli. 2023. Intramuscular vs Intravenous SARS-CoV-2 Neutralizing Antibody Sotrovimab for Treatment of COVID-19 (COMET-TAIL): A Randomized Noninferiority Clinical Trial. *Open Forum Infect. Dis.* 10:ofad354.
11. Amani, B., and B. Amani. 2022. Efficacy and safety of sotrovimab in patients with COVID-19: A rapid review and meta-analysis. *Rev. Med. Virol.* 32:e2402.
12. Rotondo, J. C., F. Martini, …, C. Contini. 2021. SARS-CoV-2 Infection: New Molecular, Phylogenetic, and Pathogenetic Insights. Efficacy of Current Vaccines and the Potential Risk of Variants. *Viruses.* 13:1687.
13. Ravi, N., D. L. Cortade, …, S. X. Wang. 2020. Diagnostics for SARS-CoV-2 detection: A comprehensive review of the FDA-EUA COVID-19 testing landscape. *Biosens. Bioelectron.* 165:112454.
14. Rahman, S., M. T. V. Montero, …, F. Kunik. 2021. Epidemiology, pathogenesis, clinical presentations, diagnosis and treatment of COVID-19: a review of current evidence. *Expert Rev. Clin. Pharmacol.* 14:601–621.
15. Hérate, C., R. Marlin, …, R. Le Grand. 2023. Sotrovimab retains activity against SARS-CoV-2 omicron variant BQ.1.1 in a non-human primate model. *Heliyon.* 9:e16664.
16. Focosi, D., A. Casadevall, …, F. Maggi. 2024. Sotrovimab: A Review of Its Efficacy against SARS-CoV-2 Variants. *Viruses.* 16:217.
17. Zhou, H., B. M. Dcosta, …, T. Tada. 2022. Resistance of SARS-CoV-2 Omicron BA.1 and BA.2 Variants to Vaccine-Elicited Sera and Therapeutic Monoclonal Antibodies. *Viruses.* 14:1334.
18. Tada, T., H. Zhou, …, N. R. Landau. 2022. Increased resistance of SARS-CoV-2 Omicron variant to neutralization by vaccine-elicited and therapeutic antibodies. *EBioMedicine.* 78:103944.
19. Kreye, J., S. M. Reincke, …, H. Prüss. 2023. Preclinical safety and efficacy of a therapeutic antibody that targets SARS-CoV-2 at the sotrovimab face but is escaped by Omicron. *iScience.* 26:106323.
20. Yetmar, Z. A., J. D. Yao, and R. R. Razonable. 2023. SARS-CoV-2 spike codon mutations and risk of hospitalization after antispike monoclonal antibody therapy in solid organ transplant recipients. *J. Med. Virol.* 95:e28885.
21. Chiang, H.-L., K.-H. Liang, …, H.-C. Wu. 2023. Broadly neutralizing human antibodies against Omicron subvariants of SARS-CoV-2. *J. Biomed. Sci.* 30:59.
22. Hu, Y.-F., J.-C. Hu, …, J.-D. Huang. 2022. In-Silico Analysis of Monoclonal Antibodies against SARS-CoV-2 Omicron. *Viruses.* 14:390.
23. Greaney, A. J., T. N. Starr, …, J. D. Bloom. 2021. Mapping mutations to the SARS-CoV-2 RBD that escape binding by different classes of antibodies. *Nat. Commun.* 12:4196.
24. Uddin, T. M., A. J. Chakraborty, …, N. Koirala. 2021. Antibiotic resistance in microbes: History, mechanisms, therapeutic strategies and future prospects. *J. Infect. Public Health.* 14:1750–1766.
25. Birnie, E., J. J. Biemond, …, W. J. Wiersinga. 2022. Development of Resistance-Associated Mutations After Sotrovimab Administration in High-risk Individuals Infected With the SARS-CoV-2 Omicron Variant. *JAMA.* 328:1104–1107.
26. Rockett, R., K. Basile, …, V. Sintchenko. 2022. Resistance Mutations in SARS-CoV-2 Delta Variant after Sotrovimab Use. *N. Engl. J. Med.* 386:1477–1479.
27. Focosi, D., S. McConnell, …, A. Casadevall. 2023. Analysis of SARS-CoV-2 mutations associated with resistance to therapeutic monoclonal antibodies that emerge after treatment. *Drug Resist. Updat.* 71:100991.
28. Palomino-Cabrera, R., F. Tejerina; …, Gregorio Marañón Microbiology-ID COVID 19 Study Group. 2023. Frequent Emergence of Resistance Mutations Following Complex Intra-Host Genomic Dynamics in SARS-CoV-2 Patients Receiving Sotrovimab. *Antimicrob. Agents Chemother.* 67:e0026623.
29. Zou, J., L. Li, …, J. He. 2022. Ultrapotent neutralizing antibodies against SARS-CoV-2 with a high degree of mutation resistance. *J. Clin. Investig.* 132:e154987.
30. McCallum, M., N. Czudnochowski, …, D. Veesler. 2022. Structural basis of SARS-CoV-2 Omicron immune evasion and receptor engagement. *Science.* 375:864–868.
31. Vilar, S., G. Cozza, and S. Moro. 2008. Medicinal chemistry and the molecular operating environment (MOE): application of QSAR and molecular docking to drug discovery. *Curr. Top. Med. Chem.* 8:1555–1572.
32. Padhi, A. K., and T. Tripathi. 2023. A comprehensive protein design protocol to identify resistance mutations and signatures of adaptation in pathogens. *Brief. Funct. Genomics.* 22:195–203.
33. Drake, Z. C., J. T. Seffernick, and S. Lindert. 2022. Protein complex prediction using Rosetta, AlphaFold, and mass spectrometry covalent labeling. *Nat. Commun.* 13:7846.
34. Maurya, S., S. Kumar, and A. K. Padhi. 2023. Interface-Guided Computational Protein Design Reveals Bebtelovimab-Resistance Mutations in SARS-CoV-2 RBD: Correlation with Global Viral Genomes and Bebtelovimab-Escape Mutations. *ChemistrySelect.* 8:e202302906.
35. Gromiha, M. M., K. Yugandhar, and S. Jemimah. 2017. Protein-protein interactions: scoring schemes and binding affinity. *Curr. Opin. Struct. Biol.* 44:31–38.
36. Kalita, P., T. Tripathi, and A. K. Padhi. 2023. Computational Protein Design for COVID-19 Research and Emerging Therapeutics. *ACS Cent. Sci.* 9:602–613.

37. Kuhlman, B. 2019. Designing protein structures and complexes with the molecular modeling program Rosetta. *J. Biol. Chem.* 294:19436–19443.
38. Saven, J. G. 2010. Computational protein design: Advances in the design and redesign of biomolecular nanostructures. *Curr. Opin. Colloid Interface Sci.* 15:13–17.
39. Samish, I. 2017. The Framework of Computational Protein Design. *Methods Mol. Biol.* 1529:3–19.
40. Fleishman, S. J., A. Leaver-Fay, …, D. Baker. 2011. RosettaScripts: a scripting language interface to the Rosetta macromolecular modeling suite. *PLoS One.* 6:e20161.
41. Crooks, G. E., G. Hon, …, S. E. Brenner. 2004. WebLogo: a sequence logo generator. *Genome Res.* 14:1188–1190.
42. Xue, L. C., J. P. Rodrigues, …, A. Vangone. 2016. PRODIGY: a web server for predicting the binding affinity of protein–protein complexes. *Bioinformatics.* 32:3676–3678.
43. Testas, A. 2023. Gradient-boosted tree regression with Pandas, Scikit-Learn, and PySpark. Distributed Machine Learning with PySpark. Apress. https://doi.org/10.1007/978-1-4842-9751-3_6.
44. Gökçe, M. M., and E. Duman. 2024. A deep learning-based demand forecasting system for planning electricity generation. *Kahramanmaraş Sütçü İmam Üniversitesi Mühendislik Bilimleri Dergisi.* 27:511–522.
45. Shehadeh, A., O. Alshboul, …, O. Hamedat. 2021. Machine learning models for predicting the residual value of heavy construction equipment: An evaluation of modified decision tree, LightGBM, and XGBoost regression. *Autom. Constr.* 129:103827.
46. Li, S., and M. Si. 2022. A comparison between linear regression, lasso regression, decision tree, XGBoost, and RNN for asset price strategies. *In* Other Conferences, *104*.
47. Singh, S., A. Gupta, T. V. Nguyen…, 2023. Multi-output career prediction: dataset, method, and benchmark suite. *In* 2023 57th Annual Conference on Information Sciences and Systems, CISS 2023 IEEE, pp. 1–6. https://doi.org/10.1109/CISS56502.2023.10089642.
48. Cen, L. P., T. K. Ng, …, M. Zhang. 2023. Artificial Intelligence-based database for prediction of protein structure and their alterations in ocular diseases. *Database.* 2023:baad083.
49. Jumper, J., R. Evans, …, D. Hassabis. 2021. Highly accurate protein structure prediction with AlphaFold. *Nature.* 596:583–589.
50. Agirre, J., M. Atanasova, …, K. Yamashita. 2023. The CCP4 suite: integrative software for macromolecular crystallography. *Acta Crystallogr. D Struct. Biol.* 79:449–461.
51. Maier, J. A., C. Martinez, …, C. Simmerling. 2015. ff14SB: Improving the Accuracy of Protein Side Chain and Backbone Parameters from ff99SB. *J. Chem. Theory Comput.* 11:3696–3713.
52. Kar, R. K., A.-F. Miller, …, M.-A. Miller. 2022. Understanding flavin electronic structure and spectra. *WIREs Comput. Mol. Sci.* 12:e1541.
53. Kar, R. K. 2023. Benefits of hybrid QM/MM over traditional classical mechanics in pharmaceutical systems. *Drug Discov. Today.* 28:103374.
54. Kossmann, S., and F. Neese. 2010. Efficient Structure Optimization with Second-Order Many-Body Perturbation Theory: The RIJCOSX-MP2 Method. *J. Chem. Theory Comput.* 6:2325–2338.
55. Grimme, S., S. Ehrlich, and L. Goerigk. 2011. Effect of the damping function in dispersion corrected density functional theory. *J. Comput. Chem.* 32:1456–1465.
56. Sherwood, P., A. H. de Vries, …, C. Lennartz. 2003. QUASI: A general purpose implementation of the QM/MM approach and its application to problems in catalysis. *J. Mol. Struct.: THEOCHEM.* 632:1–28.
57. Neese, F. 2023. The SHARK integral generation and digestion system. *J. Comput. Chem.* 44:381–396.
58. Perlmutter, J. D., W. J. Drasler, …, J. N. Sachs. 2011. All-atom and coarse-grained molecular dynamics simulations of a membrane protein stabilizing polymer. *Langmuir.* 27:10523–10537.
59. Alessandri, R., J. Barnoud, …, S. J. Marrink. 2022. Martini 3 Coarse-Grained Force Field: Small Molecules. *Adv. Theory Simul.* 5:2100391.
60. Halonen, R., I. Neefjes, and B. Reischl. 2023. Further cautionary tales on thermostatting in molecular dynamics: Energy equipartitioning and non-equilibrium processes in gas-phase simulations. *J. Chem. Phys.* 158:194301.
61. Lemak, A. S., and N. K. Balabaev. 1994. On The Berendsen Thermostat. *Mol. Simul.* 13:177–187.
62. Martoňák, R., A. Laio, and M. Parrinello. 2003. Predicting Crystal Structures: The Parrinello-Rahman Method Revisited. *Phys. Rev. Lett.* 90:4.
63. Watanabe, Y., J. D. Allen, …, M. Crispin. 2020. Site-specific glycan analysis of the SARS-CoV-2 spike. *Science.* 369:330–333.
64. Jo, S., T. Kim, …, W. Im. 2008. CHARMM-GUI: A web-based graphical user interface for CHARMM. *J. Comput. Chem.* 29:1859–1865.
65. Park, S. J., J. Lee, …, W. Im. 2019. CHARMM-GUI Glycan Modeler for modeling and simulation of carbohydrates and glycoconjugates. *Glycobiology (Oxf.).* 29:320–331.
66. Hess, B., H. Bekker, …, J. G. Fraaije. 1997. LINCS: A linear constraint solver for molecular simulations. *J. Comput. Chem.* 18:1463–1472, Wiley Online Library.
67. Darden, T., D. York, and L. Pedersen. 1993. Particle mesh Ewald: An N·log(N) method for Ewald sums in large systems. *J. Chem. Phys.* 98:10089–10092.
68. Ma, S., and Y. Dai. 2011. Principal component analysis based Methods in bioinformatics studies. *Brief. Bioinform.* 12:714–722.
69. Valdés-Tresanco, M. S., M. E. Valdés-Tresanco, …, E. Moreno. 2021. Gmx_MMPBSA: A New Tool to Perform End-State Free Energy Calculations with GROMACS. *J. Chem. Theory Comput.* 17:6281–6291.
70. Venkatakrishnan, A. J., R. Fonseca, …, R. O. Dror. 2019. Uncovering patterns of atomic interactions in static and dynamic structures of proteins. Preprint at bioRxiv. https://doi.org/10.1101/840694.
71. Niranjan, V., P. Rao, …, J. Kumar. 2023. Protocol for the development of coarse-grained structures for macromolecular simulation using GROMACS. *PLoS One.* 18:e0288264.
72. Abraham, M. J., T. Murtola, …, E. Lindahl. 2015. GROMACS: High performance molecular simulations through multi-level parallelism from laptops to supercomputers. *SoftwareX.* 1–2:19–25.
73. Sukhwal, A., and R. Sowdhamini. 2013. Oligomerisation status and evolutionary conservation of interfaces of protein structural domain superfamilies. *Mol. Biosyst.* 9:1652–1661.
74. Server, W., O. K. Mathew, and R. Sowdhamini. 2016. PIMA: Protein-Protein interactions in Macromolecular Assembly - a web server for its Analysis and Visualization. *Bioinformation.* 12:9.
75. Singer, J., R. Gifford, …, D. Robertson. 2020. CoV-GLUE: A Web Application for Tracking SARS-CoV-2 Genomic Variation.
76. Lee, S. J., Y.-J. Kim, and D.-G. Ahn. 2022. Distinct Molecular Mechanisms Characterizing Pathogenesis of SARS-CoV-2. *J. Microbiol. Biotechnol.* 32:1073–1085.
77. Rochman, N. D., Y. I. Wolf, …, E. V. Koonin. 2021. Ongoing Global and Regional Adaptive Evolution of SARS-CoV-2. Preprint at bioRxiv. https://doi.org/10.1101/2020.10.12.336644.
78. Bloom, J. D., A. C. Beichman, …, K. Harris. 2023. Evolution of the SARS-CoV-2 Mutational Spectrum. *Mol. Biol. Evol.* 40:msad085.
79. Pinto, D., Y. J. Park, …, D. Corti. 2020. Cross-neutralization of SARS-CoV-2 by a human monoclonal SARS-CoV antibody. *Nature.* 583:290–295.
80. Cathcart, A. L., C. Havenar-Daughton, …, C. M. Hebner. 2022. The dual function monoclonal antibodies VIR-7831 and VIR-7832 demonstrate potent in vitro and in vivo activity against SARS-CoV-2. Preprint at bioRxiv. https://doi.org/10.1101/2021.03.09.434607.

81. Ragonnet-Cronin, M., R. Nutalai, …, S. Rokadiya. 2023. Generation of SARS-CoV-2 escape mutations by monoclonal antibody therapy. *Nat. Commun.* 14:3334.

82. Andrés, C., A. González-Sánchez, …, A. Antón. 2023. Emergence of Delta and Omicron variants carrying resistance-associated mutations in immunocompromised patients undergoing sotrovimab treatment with long-term viral excretion. *Clin. Microbiol. Infection.* 29:240–246.

83. Doggrell, S. A. 2021. Do we need bamlanivimab? Is etesevimab a key to treating Covid-19? *Expert Opin. Biol. Ther.* 21:1359–1362.

84. Kumar, P., X. Zhang, …, M. Dobbelstein. 2024. Identification of antibody-resistant SARS-CoV-2 mutants via N4-Hydroxycytidine mutagenesis. *Antiviral Res.* 231:106006.

85. Liu, M., H. Gan, …, B. Sun. 2023. Review of therapeutic mechanisms and applications based on SARS-CoV-2 neutralizing antibodies. *Front. Microbiol.* 14:1122868.

86. Taylor, P. C., A. C. Adams, …, R. L. Gottlieb. 2021. Neutralizing monoclonal antibodies for treatment of COVID-19. *Nat. Rev. Immunol.* 21:382–393.